Calcium-Mediated Nitrogen Reduction for Electrochemical Ammonia Synthesis

Xianbiao Fu,[1†] Valerie A. Niemann,[2†] Yuanyuan Zhou,[1†] Shaofeng Li,[1] Ke Zhang,[1] Jakob B. Pedersen,[1] Mattia Saccoccio,[1] Suzanne Z. Andersen,[1] Kasper Enemark-Rasmussen,[3] Peter Benedek,[2] Aoni Xu,[1] Niklas H. Deissler,[1] Jon Bjarke Valbæk Mygind,[1] Adam C. Nielander,[4] Jakob Kibsgaard,[1] Peter C. K. Vesborg,[1] Jens K. Nørskov,[1*] Thomas F. Jaramillo,[2*] Ib Chorkendorff[1*]

[1]Department of Physics, Technical University of Denmark, Kongens Lyngby, Denmark

[2]Department of Chemical Engineering, Stanford University, 443 Via Ortega, Stanford, California 94305, United States

[3]Department of Chemistry, Technical University of Denmark, Kongens Lyngby, Denmark

[4]SUNCAT Center for Interface Science and Catalysis, SLAC National Accelerator Laboratory, Menlo Park, CA, 94025, USA

*Corresponding author.

Email: jkno@dtu.dk (J.K.N.), jaramillo@stanford.edu (T.J.), ibchork@fysik.dtu.dk (I.C.)

†These authors contributed equally to this work

Introductory Paragraph

Ammonia (NH_3) is a feedstock chemical for fertilizers, nitrogen-containing organic chemicals, pharmaceuticals, and polymers, but its industrial synthesis via the Haber-Bosch process accounts for 1.3% of global carbon dioxide emissions.[1-5] Electrochemical ammonia synthesis is a complementary route for the de-localized production of NH_3 powered by renewable energy.[6,7] The first verified electrochemical method is a lithium (Li)-mediated process in organic electrolytes.[6,7] To date, only metallic Li has been used for this process, and other elements remain to be explored for potential benefits in efficiency, reaction rates, device design, abundance, and stability. In the first demonstration of a lithium-free system, we found that calcium, the fifth most abundant crustal element (2500 times that of lithium),[8] can mediate ammonia synthesis. We achieved an ammonia Faradaic efficiency of 40 ± 2% using calcium tetrakis(hexafluoroisopropyloxy)borate

($Ca[B(hfip)_4]_2$) as the electrolyte. Our results open the possibility of using abundant materials for the electrochemical production of fertilizer.

The global industrial production of NH_3 through the Haber-Bosch process was 182 million metric tons in 2021.[4] However, the Haber-Bosch process requires extreme reaction conditions (*i.e.,* 150 - 200 bar, and 350 - 450 °C), consumes roughly 1% of the global energy supply, and contributes over 1.3% of global carbon dioxide emissions.[5] Thus, many attempts have been made to explore sustainable approaches for ammonia synthesis under milder conditions.[3] Aqueous methods have been subject to ammonia contamination, however, and to date, the lithium-mediated nitrogen reduction reaction (Li-NRR) in organic solvent has been identified as one of the most reliable routes for electrochemical ammonia synthesis.[6,7] The Li-NRR system was the first reported in 1930 by Fichter *et al.* and further explored by Tsuneto *et al.* via optimizing electrolytes, albeit none of them followed up on their work.[9-11] Our groups validated Li-NRR through a rigorous protocol with quantitative isotope measurements to prove that NH_3 is produced from N_2 reduction.[7]

Extensive work has focused on improving the performance of the Li-NRR system for ammonia synthesis.[12-19] Faradaic efficiencies (FE) close to 100% towards ammonia and current densities up to -1 A cm_{geo}^{-2} have been achieved in pressurized batch systems (15 bar or 20 bar) by regulating the electrode-electrolyte interface and using high surface area electrodes, respectively.[20,21] These achievements are only obtained, however, by using sacrificial proton donors. Very recently, we achieved continuous-flow electrosynthesis of ammonia by nitrogen reduction coupled with hydrogen oxidation at ambient pressure and temperature with a Faradaic efficiency of 61 ± 1%.[22] Currently, Li is the only material demonstrated to work in this process, and thus it is necessary to expand the repertoire of available materials for potential gains in energy efficiency, reaction rates,

stability, device design, and cost. An example of a potential challenge with the Li-based system is competition with lithium-based batteries for scarce lithium resources. The continuous-flow reactor provides a new platform to explore beyond lithium for electrochemical ammonia synthesis.

We identified calcium (Ca), the fifth most prevalent element in the Earth's crust with an abundance of 4.7 %, to be a promising alternative to lithium.[8] In the early 20th century, the Frank-Caro process was developed to produce ammonia by reacting calcium carbide (CaC_2) with N_2 at 1,000 °C to form calcium cyanamide ($CaCN_2$) which was subsequently hydrolyzed to release ammonia.[23] Harder and co-workers reported that the low-valent Ca complex could activate N_2 at low temperatures (0 ^{o}C).[24] Calcium metalate catalysts have been investigated for N_2 reduction in aqueous electrolytes, but without rigorous gas purification and quantitative isotope measurements, it is unproven that the produced NH_3 is from N_2 reduction.[25] To the best of our knowledge, there is still no verified, reproducible result for aqueous N_2 reduction to ammonia.[6,7,26] Experimentally, we demonstrated that metallic Ca film can chemically activate N_2 at room temperature and 1 bar pressure (Figures S1, S2 and Supplementary Text). Additionally, the standard reduction potential of Ca is -2.87 V vs. the standard hydrogen electrode (SHE), close to that of Li (-3.04 V vs. SHE). These factors suggest that metallic Ca is amenable to electroplating from solution and activates N_2 at room temperature. Inspired by investigations of calcium metal batteries, we found that Ca electroplating and stripping can be achieved in electrolytes containing $Ca[B(hfip)_4]_2$ and calcium borohydride ($Ca(BH_4)_2$) in tetrahydrofuran (THF) at 1 bar and room temperature.[27-35] Typical Li-based electrolytes were composed of lithium perchlorate ($LiClO_4$) and lithium tetrafluoroborate ($LiBF_4$) dissolved in THF, but the calcium versions of these salts, calcium perchlorate ($Ca(ClO_4)_2$) and calcium tetrafluoroborate ($Ca(BF_4)_2$), are poorly soluble in THF. Previous work has indicated,

however, that $Ca(ClO_4)_2$ and $Ca(BF_4)_2$ can achieve Ca plating and stripping in ethylene carbonate (EC) and propylene (PC) at 75 - 100 °C.[31]

In this letter, we demonstrate the first metal alternative to lithium for electrochemically driven nitrogen reduction to ammonia. We achieved a calcium-mediated nitrogen reduction reaction (Ca-NRR) using $Ca[B(hfip)_4]_2$ or $Ca(BH_4)_2$ dissolved in THF with 0.25 vol.% by ethanol (EtOH) as a proton shuttle at ambient conditions. The ammonia FEs of $Ca[B(hfip)_4]_2$ and $Ca(BH_4)_2$ electrolytes were 40 ± 2% and 28 ± 3%, respectively, at 1 bar and room temperature. Ar-fed experiments and quantitative $^{15}N_2$ isotope measurements confirmed that the synthesized ammonia came from N_2 reduction.

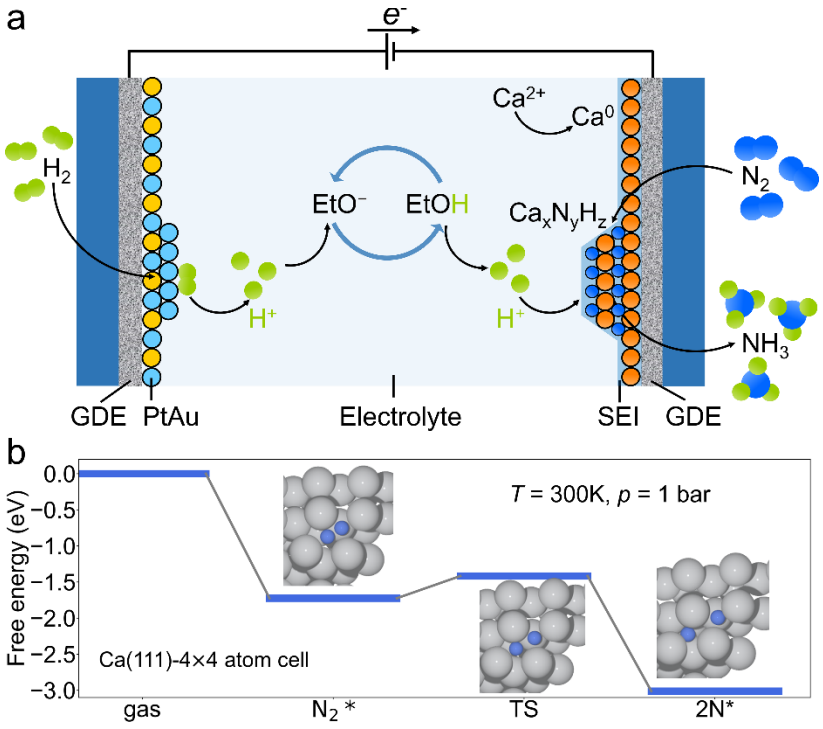

Figure 1. Investigation of calcium-mediated nitrogen reduction. (a) Schematic of Ca-NRR in a flow cell. The Ca^{2+} diffuses from the bulk electrolyte through the solid-electrolyte interphase (SEI) and is reduced to metallic Ca on the cathode. Metallic Ca reacts with N_2 to form calcium

nitride ($Ca_xN_yH_z$) which is then protonated to produce ammonia. A Pt-enriched PtAu alloy is used as the anode hydrogen oxidation reaction (HOR) catalyst.[22] (b) Free energy diagram for nitrogen adsorption and dissociation on the Ca(111) surface.

Ca-NRR was carried out in a three-chamber flow cell at 1 bar and room temperature, and the effective area of the flow field was 25 cm^2.[22] Figure 1a depicts the cathode side, on which the calcium ion (Ca^{2+}) is electrochemically reduced into metallic calcium which then reacts with N_2 to form calcium nitride ($Ca_xN_yH_z$) (Figure S3). On the anode side, the hydrogen oxidation reaction (HOR) on the PtAu alloy catalysts continuously provides protons for Ca-NRR, transported by a proton shuttle, which in this case is ethanol (EtOH). Finally, the calcium nitride is protonated by EtOH to continuously produce ammonia. Our theoretical calculations reveal a relatively low N_2 dissociation barrier on the metallic calcium surface, indicating that the nitrogen dissociation on the calcium is fast at ambient conditions (Figure 1b), which is consistent with our experimental results that metallic Ca exhibited the capacity to activate N_2 at room temperature (Figure S1 and S2). Both the surface vibration modes and the dipole-field contributions (Table S1) are included in the free energy barrier. The calculated dissociation barrier varies within 0.1 eV in the presence of the SEI layer contacting with the THF solvent (Figure S4). Furthermore, unlike transition metals, on one hand, calcium and lithium exhibit facile nitrogen dissociation barrier (Figure S5), and on the other hand, the close-to-zero NH_3 adsorption energy (Table S2) helps to desorb the produced NH_3 easily at ambient conditions. The reduced calcium surface can partially transform into a hydride (N_2-limiting region) or nitride (proton-limiting region) due to the significant thermodynamic driving force (Figure S6 and Table S3). In the optimal region, the cathodic surface remains as the metallic calcium surface (Figure S7), The electrochemical barriers for hydrogen evolution and N_2 reduction

are estimated to be facile at the very negative potential (Figures S8, S9, and Table S4). Therefore, we conclude that Ca-NRR is also a mass-transport-limited reaction, similar to Li-NRR (See Supplementary for detailed discussion). The stainless-steel cloth (SSC) was used as a gas diffusion electrode (GDE) to overcome the mass transport limitation of N_2 and H_2. The working electrode (WE, cathode) and counter electrode (CE, anode) were SSC with a pore size of 30 μm (Figure S10), and the PtAu alloy catalysts on the SSC substrate (PtAu/SSC), respectively. The pseudo reference electrode (RE) was a Pt wire. The N_2 and H_2 used in the experiments were cleaned by commercial purifiers (NuPure) to reduce N-containing compounds to the parts per trillion by volume (ppt-v) level (Figure S11). The gas flow rates were controlled by a mass flow controller (Brooks Instrument). The pressure gradient between the gas inlet and outlet was fixed at approximately 15 mbar to prevent electrolyte flooding into the gas side of the GDE (Figure S11). The electrolyte consisted of 0.2 M $Ca[B(hfip)_4]_2$ or 0.5 M $Ca(BH_4)_2$ in THF with 0.25 vol.% EtOH as the proton shuttle. Typically, the produced ammonia was distributed in the gas phase, electrolyte, and electrode deposits. The ammonia content was measured using ion chromatography (IC, Metrohm).

$Ca[B(hfip)_4]_2$ was synthesized by reacting $Ca(BH_4)_2$ with hexafluoroisopropanol (hfip) as previously reported.[32,33] The as-prepared $Ca[B(hfip)_4]_2$ was characterized by nuclear magnetic resonance (NMR) (Figures S12 and S13). The performance of four calcium salts was examined in the flow cell and single-compartment cell at room temperature, first by demonstrating Ca plating onto the cathode. As shown in Figure 2a, Ca plating onto the cathode was observed in the cyclic voltammograms (CV) of $Ca[B(hfip)_4]_2$ and $Ca(BH_4)_2$ in the flow cell, as well as in the CV in the single cell (Figures S14 and S15). The CV of $Ca(BH_4)_2$ shows the Ca plating at around -2 V vs.

Pt, where the plating onset potential may have been shifted due to a potential shift of the reference electrode of Pt. The onset potential in the single-compartment cell with a lithium iron phosphate (LFP) reference shows a Ca plating closer to -3 V vs LFP, the expected plating potential value (Figure S14).[36] The sharp Ca plating curve of $Ca[B(hfip)_4]_2$ can be attributed to its higher ionic conductivity compared to $Ca(BH_4)_2$ (Figures S14-S17). Ca battery studies show Ca plating and stripping to be less reversible than Li due to the presence of Ca-containing deposits or passivation layer on the electrode, however, electrochemical Ca stripping is not required for ammonia production.[27,29-31,33-35] Under similar conditions, the masses of deposits on the cathode for the Li-NRR and Ca-NRR experiments are not significantly different (Figure S18). Chronopotentiometry (CP) of $Ca[B(hfip)_4]_2$ was conducted at a current density of -2 mA/cm^2 (Figure 2b). The anode potential remained at ~0.3 V vs. Pt and the cathode potential stabilized at ~-4.5 V vs. Pt. After passing 200 C of charge, the ammonia FEs of 33 ± 1% was achieved without potential cycling (Figure 2c), and about 90% of the produced ammonia was distributed in the electrolyte (Figure 2d). The CP of $Ca(BH_4)_2$ in THF with EtOH was conducted with the current density of -0.8 mA/cm^2 (Figure S19). The $Ca(BH_4)_2$ exhibited an ammonia FE of 28 ± 3% after passing 100 C (Figure 2c). Most of the detected ammonia originated from the electrode deposits (Figure 2d), suggesting that Ca-NRR with $Ca(BH_4)_2$ may operate in the proton-limiting regime,[12,22] where $Ca(BH_4)_2$ consumes protons by reacting with EtOH and protons produced from HOR, confirmed by NMR data (Figure S20). In other words, available protons were consumed by $Ca(BH_4)_2$, leading to a deficit in protons available to protonate the calcium nitride and form ammonia — consistent with the known reactivity of the BH_4^- anion in the presence of a proton source. NH_3 was produced by hydrolyzing the calcium nitride in a batch process similar to a previously reported Li cycling procedure.[17] After disassembling the flow cell, black electrode deposits were observed on the

cathode (Figure S21), corroborating the Ca plating observed in the CV curve (Figure 2a). Moreover, no ammonia can be detected when using Ar as the cathode gas, which suggested that the produced NH_3 is from reduction of N_2 when feeding N_2 (Figure 2c). CP experiments of $Ca(BH_4)_2$ and $Ca[B(hfip)_4]_2$ were also conducted in a single-compartment cell with SSC as a working electrode, LFP as a reference electrode, and Pt mesh as a counter electrode (Figures S22 and S23). In single-compartment cell experiments, 6.3% FE in the SEI and 3.6% FE in the electrolyte were detected by using $Ca(BH_4)_2$ and $Ca[B(hfip)_4]_2$, respectively.

CVs of $Ca(ClO_4)_2$ and $Ca(BF_4)_2$) show a much lower current density even with an applied potential up to -5 V vs. Pt, and they do not show evidence of Ca stripping (Figure 2a). The CP experiments of $Ca(ClO_4)_2$ and $Ca(BF_4)_2$ were conducted at a current density of -0.25 mA/cm^2 (Figures S24 and S25). After 30 minutes of CP, the cathode potentials were more negative than -15 V vs. Pt, suggesting no Ca plating on the cathode. This result agrees with the previous findings that Ca does not plate from dissolved $Ca(ClO_4)_2$ or $Ca(BF_4)_2$ at room temperature.[31] The ability of Ca to plate from a salt may relate to the Ca^{2+} conductivity of the SEI layer and the energy barrier for Ca nucleation and growth.[31] No ammonia was detected after the CP experiments using $Ca(ClO_4)_2$ and $Ca(BF_4)_2$ as electrolyte salts (Figure 2c).

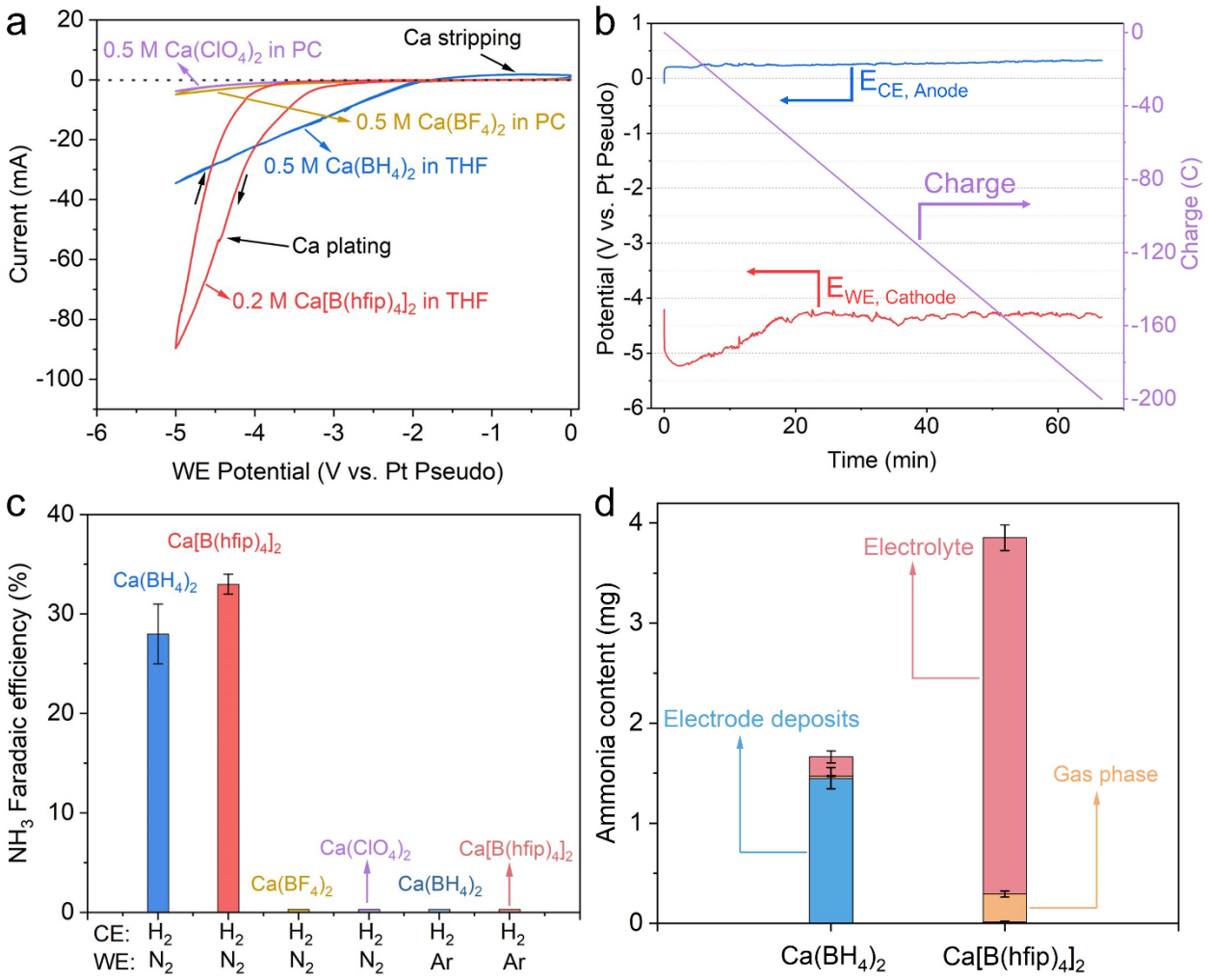

Figure 2. Electrochemical tests of Ca-NRR in the flow cell. (a) Cyclic voltammetry (CV) curves were recorded between 0 V and -5 V vs. Pt with a scan rate of 20 mV/s without iR correction. The electrode area was 25 cm^2. The electrolytes were 0.2 M $Ca[B(hfip)_4]_2$ in THF, 0.5 M $Ca(BH_4)_2$ in THF, $Ca(ClO_4)_2$ in PC, and $Ca(BF_4)_2$ in PC with 0.25 vol.% EtOH. (b) Chronopotentiometry (CP) of $Ca[B(hfip)_4]_2$ at a current density of -2 mA/cm^2 (current: -50 mA). All potentials reported are shown without iR correction. The electrolyte comprised 0.2 M $Ca[B(hfip)_4]_2$ in THF with 0.25 vol.% EtOH. (c) Ammonia Faradaic efficiencies of different calcium salts under control experimental conditions. CE and WE represent counter electrode (anode) and working electrode (cathode) side gas feeding, respectively. (d) The distribution of

produced ammonia in the electrolyte, gas phase, and electrode deposits. The total passed charge for 0.2 M $Ca[B(hfip)_4]_2$ and 0.5 M $Ca(BH_4)_2$ was 200 C and 100 C, respectively. In the case of $Ca(BH_4)_2$, it should be noted that H_2O can react with N-containing compounds (e.g. $Ca_xN_yH_z$) in the electrode deposits to produce NH_3. Error bars represent the standard deviation from at least three independent measurements.

To confirm that the produced ammonia came from nitrogen reduction, $^{15}N_2$ (Sigma Aldrich, 98 at.% purity, cleaned by purifier) isotopic labelling experiments were employed in the flow cell under the same conditions as the $^{14}N_2$ experiments (Figure S26) for the electrolyte comprising of 0.2 M $Ca[B(hfip)_4]_2$ in THF with 0.25 vol.% EtOH. Two independent experiments were performed after passing charges of 60 C and 200 C, respectively. When the electrolyte was directly measured after the experiment using ^{1}H NMR, a peak at 7 ppm covered the peaks of NH_4^+, and therefore, the electrolyte had to be diluted 5-10 times by 2 M HCl to distinguish the ammonia peak (Figure S27). This diluted solution was used for the ^{1}H NMR measurement with acetone as the calibration compound. As shown in Figure 3a, the doublet $^{15}NH_4^+$ signals of both the electrolyte and gas phase for the experiments strongly suggest that the ammonia was produced from the reduction of N_2. The $^{15}NH_4^+$ was also quantified by ion chromatography. The quantified concentrations of $^{15}NH_4^+$ by IC and NMR were very similar, confirming the reliability of the quantification method (Figure 3b). Moreover, similar amounts of ammonia were synthesized in both $^{15}N_2$ and $^{14}N_2$ experiments under matching conditions, indicating that the detected ammonia originated from N_2 reduction by the Ca-NRR process (Table S5 and Figure S28). For the $Ca[B(hfip)_4]_2$ salt, the ammonia in the electrode deposits solution was less than 0.5% of the total produced ammonia (Table S5). Thus, the electrode deposits solution was not tested for NMR analysis.

After confirming that the synthesized NH_3 came from N_2 reduction, a method to enhance NH_3 selectivity was investigated. While 33 ± 1% FE towards NH_3 is comparable with recent Li-NRR reports in the literature (Table 6), there is a need to mitigate competing side reactions, including Ca reaction with protons to form products such as H_2 and calcium hydride (CaH_2). We demonstrated that once the metallic Ca has formed CaH_2, it loses its unique ability to activate N_2 at room temperature (i.e., CaH_2 cannot activate N_2 at room temperature), which accounts for some loss of FE in the Ca-NRR process (Figure S29). The effect of EtOH concentration on the NH_3 FE revealed that protons compete with N_2 for reacting with deposited Ca metal, and the reaction between Ca metal and protons is dominated in the N_2-limited region (high EtOH concentration), leading to decreasing NH_3 selectivity (Figures S30 and S31). Potential cycling was employed in a proton-limited regime (0.25 vol% EtOH) to facilitate Ca reaction with N_2, and then NH_3 formation coupled with Ca dissolution, as has been demonstrated in Li-NRR literature and investigated using atomistic kinetic modeling.[22] As a result, an enhancement of NH_3 selectivity to a FE of 40 ± 2% was observed (Figure S32). It is evident when comparing the effect of ethanol concentration between Ca-NRR and Li-NRR that the optimal ethanol concentration ranges are broader for Ca-NRR. Ca-NRR likely requires more ethanol to disrupt the solid electrolyte interphase layer and expose the freshly plated, metallic Ca for N_2 activation. This requirement may explain some loss of FE for the Ca-NRR system compared to the Li-NRR system (Figure S30). [22,31]Additional methods must be considered to further enhance the NH_3 selectivity, including increasing temperature[23] and designing Ca complexation schemes.[24] In the Li-NRR system, SEI engineering and reactor design has drastically improved selectivity, and these methods may translate to the Ca-NRR system. Competition between side reactions and ammonia production will continue to be an area of import, both for the established Li-NRR and new Ca-NRR fields.

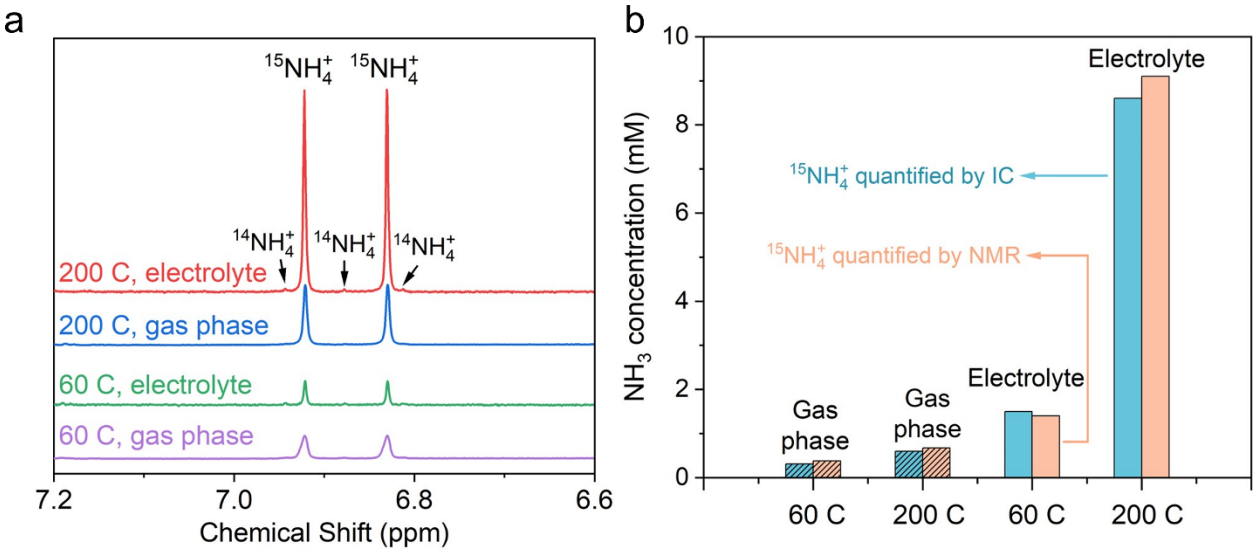

Figure 3. $^{15}N_2$ isotope labelling experiments in 0.2 M Ca[B(hfip)$_4$]$_2$ in the flow cell. (a) NMR spectra were obtained by using $^{15}N_2$, with samples taken at 60 C and 200 C from independent experiments. (b) The comparison of NH_3 concentrations quantified by IC and NMR. NH_3 concentration quantified by NMR was derived from the integration of the spectra in (a) with respect to an internal standard.

To investigate the composition of the post-reaction electrode deposits resulting from either $Ca(BH_4)_2$- or Ca[B(hfip)$_4$]$_2$-containing electrolytes (denoted as $Ca(BH_4)_2$ or Ca[B(hfip)$_4$]$_2$), X-ray photoelectron spectroscopy (XPS), scanning electron microscope (SEM), and X-ray diffraction (XRD) were employed. Ca-NRR experiments were performed in an Ar-filled glovebox, and a transfer system (Figures S33- S35) was used to minimize sample exposure to air. The SEM images of $Ca(BH_4)_2$ show thick deposits on the cathode after the CP test of 100 C charge (Figure S36). Energy dispersive spectrometry (EDS) mapping shows the uniform distribution of calcium and boron (Figure S37). On average, the EDS spectrum of electrode deposits exhibits a Ca/B ratio of 1:2, corresponding to that of $Ca(BH_4)_2$ (Figure S38). The XRD pattern of the $Ca(BH_4)_2$ electrode reveals that the main crystalline component in electrode deposits is $Ca(BH_4)_2$ (Figure S39). For

the $Ca[B(hfip)_4]_2$ experiments, the SEM images show fewer electrode deposits than $Ca(BH_4)_2$ (Figure S40). The thickness of electrode deposits likely indicates the presence of reduced nitrogen species in the electrode deposits. In other words, the thick deposits from $Ca(BH_4)_2$ may largely contain built-up reduced nitrogen species, while fewer deposits from $Ca[B(hfip)_4]_2$ support that the reduced nitrogen forms ammonia directly in the electrolyte and gas phase (Figure 2d). The EDS mapping of $Ca[B(hfip)_4]_2$ exhibits the distribution of calcium and boron (Figure S41) and the Ca/B ratio is close to 1:4 (Figure S42). Inductively coupled plasma mass spectrometry (ICP-MS) analysis of the electrode deposits showed slightly more Ca-rich ratios: 3:4 for $Ca(BH_4)_2$ and 4:5 for $Ca[B(hfip)_4]_2$, indicating Ca plating (Table S7).

Depth profiling XPS spectra of electrode deposits using $Ca(BH_4)_2$ or $Ca[B(hfip)_4]_2$ were obtained using an Ar ion gun to etch the surface at different times (Figure 4 and Figure S43). XPS survey spectra of the post-reaction electrode deposits are given in the Supporting Information (Figures S44 and S45). The adventitious C 1s peaks were calibrated to 284.8 eV (Figure S46), and other peaks were shifted accordingly. As shown in Figure 4a, the doublet peaks of Ca $2p_{1/2}$ and Ca $2p_{3/2}$ with the splitting of ~3.5 eV were observed.[37] With increasing etching time, the Ca $2p_{3/2}$ peaks were shifted to the lower binding energies, which may indicate the presence of Ca^0 in the post-reaction electrode deposits.[37] As shown in Figure 4b, the N 1s spectra of post-reaction $Ca(BH_4)_2$ electrode deposits have a peak at 398 eV, which is attributed to calcium nitride.[38] When using $Ca(BH_4)_2$ as an electrolyte, the Ca-NRR was likely in the proton-limiting region (i.e. $Ca(BH_4)_2$ reacted with EtOH to reduce available proton concentration), which led to the accumulation of calcium nitride species ($Ca_xN_yH_z$).[12,22] CaH_2 is known to form during Ca plating in $Ca(BH_4)_2$-based electrolytes.[26] CaH_2 is subject to nitridation in the presence of N_2, but only at elevated

temperatures.[39] It may also react with protic species.[40]. This XPS result is consistent with the measured ammonia produced from electrode deposits (Figure 2d) and the SEM image results (Figure S36). Compared to the post-reaction electrode deposits of $Ca(BH_4)_2$, the $Ca[B(hfip)_4]_2$ electrode deposits had a slight shift in the Ca $2p_{3/2}$ positions to higher binding energies with increasing etching time (Figure 4c). Moreover, there is no N 1s signal in the post-reaction electrode deposits of $Ca[B(hfip)_4]_2$ (Figure 4d), which agrees with the results that little ammonia (less than 20 μg) was found in the electrode deposits (Table S5). When using $Ca[B(hfip)_4]_2$ as an electrolyte and EtOH as a proton carrier, the Ca-NRR was in the nitrogen-limiting region, and the calcium nitride species were consumed by EtOH to produce NH_3.[12,22] Therefore, almost no nitrogen species were present in post-reaction electrode deposits of $Ca[B(hfip)_4]_2$. Depth-profiling XPS B 1s spectra (Figure S47) show that BO_x/BH_x and BO_x/BF_x were present in the post-reaction electrode deposits of both $Ca(BH_4)_2$ and $Ca[B(hfip)_4]_2$, respectively.[41] The thermodynamic stability analysis (i.e. free energy versus the applied potential) suggested that possibly stable solid phases in the electrode deposits are $Ca(BF_4)_2$, $Ca_xB_yO_z$, CaF_2, $Ca(OH)_2$, and CaO (Figure S48). These findings are consistent with the experimental observations. Time-series experiments were performed over 10 mins, 67 mins, 133 mins, and 267 mins to show the changes in cathode deposits during the Ca-NRR process. The NH3 Faradaic efficiencies stay around 30-33% over 4 h (Figure S49). The turnover number of Ca-NRR (0.088) is comparable with that of Li-NRR (0.075) under similar conditions (Figure S50).[22] The thickness and composition of the electrode deposits did not change significantly over time (Figure S51-54). Unique properties of the Ca electrode deposits are subject for future study.

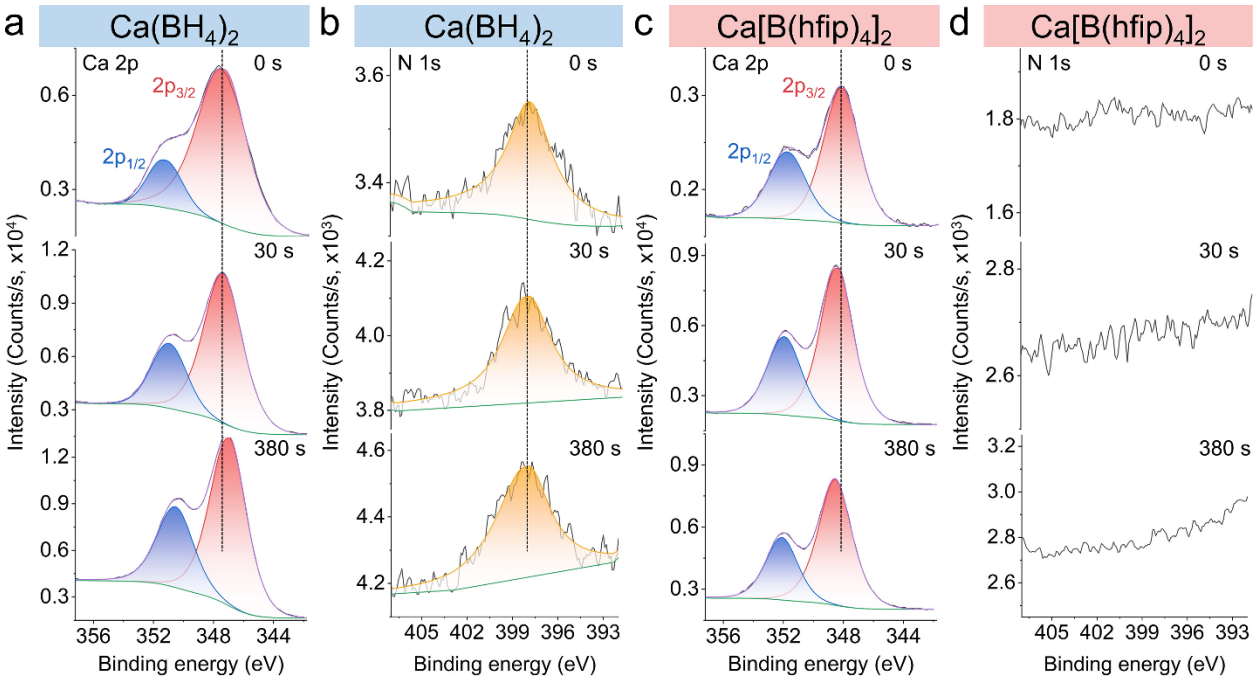

Figure 4. XPS investigation of the post-reaction cathode deposits without exposure to air at different argon sputtering times. (a and b). *Depth-profiling XPS spectra of Ca 2p* ***(a)*** *and N 1s* ***(b)*** *for the post-reaction electrode deposits of $Ca(BH_4)_2$ after the CP test of 100 C.* ***(c and d)****. Depth-profiling XPS spectra of Ca 2p* ***(c)*** *and N 1s* ***(d)*** *for the post-reaction electrode deposits of $Ca[B(hfip)_4]_2$ after the CP test of 200 C.*

In summary, we have demonstrated the first electrochemical, beyond the Li-mediated ammonia synthesis method using calcium. We found that metallic calcium can be electrodeposited onto SSC using $Ca(BH_4)_2$ as the electrolyte at room temperature, and the metallic calcium then reacts with N_2 to form $Ca_xN_yH_z$ deposits on the electrode. Dipping the $Ca_xN_yH_z$ deposits in water results in NH_3 formation, similar to a previously reported Li cycling method.[17] The resulting Faradaic efficiency of the $Ca(BH_4)_2$ batch process is 28 ± 3%. Due to the reactivity of $Ca(BH_4)_2$ with the proton shuttle EtOH during the Ca-NRR process, we synthesized another calcium salt, $Ca[B(hfip)_4]_2$, by reacting $Ca(BH_4)_2$ with hexafluoroisopropanol. Continuous calcium-mediated

ammonia synthesis was successfully achieved in a flow cell using the electrolyte containing $Ca[B(hfip)_4]_2$ dissolved in THF with EtOH as the proton shuttle. The resulting ammonia FE was 40 ± 2% at ambient conditions. Quantitative $^{15}N_2$ isotope measurements and Ar-fed experiments proved that the produced ammonia originated from the reduction of N_2 for $Ca(BH_4)_2$ and $Ca[B(hfip)_4]_2$ salts.

This work opens avenues for expanding mechanistic knowledge and solving engineering challenges in Ca-NRR. Importantly, competition between ethanol reduction and N_2 activation will require further study to enhance selectivity to NH_3. Understanding this competition would necessitate determining the composition, structure, and properties of the active Ca-rich layer, including its calcium nitride and hydride species. This work also motivates the investigation of the Ca solid electrolyte interphase (SEI) layer. Meanwhile for reactor design, it is well known that Ca^{2+} intercalation into a graphite electrode is much more difficult than Li^+, which brings the advantage that Ca-NRR may use cheaper carbon-based GDE electrodes in practical applications.[42,43] Finally, this work inspires the exploration of other metal alternatives to Li, e.g., Mg, Ba, Sr, and Na, for mediating nitrogen reduction to ammonia. These alternatives would broaden the options for efficient, selective, stable, cost-effective, and scalable technologies for electrochemical fertilizer synthesis.

Methods

Methods, experimental details, and additional figures and tables are available in Supporting Information. https://

Competing interests

The authors declare no conflict of interest.

Acknowledgments

We gratefully acknowledge the funding by Villum Fonden, part of the Villum Center for the Science of Sustainable Fuels and Chemicals (V-SUSTAIN grant 9455), Innovationsfonden (E-ammonia grant 9067-00010B), and the European Research Council (ERC) under the European Union's Horizon 2020 research and innovation programme (grant agreement No 741860). X.F. was supported under the MSCA European Postdoctoral Fellowships (Electro-Ammonia Project 101059643). V.A.N. was supported under the National Science Foundation Graduate Research Fellowship Program under Grant No. DGE – 1656518 and the Camille and Henry Dreyfus Foundation. A.C.N. was supported by the U.S. Department of Energy, Office of Science, Office of Basic Energy Sciences, Chemical Sciences, Geosciences, and Biosciences Division, Catalysis Science Program through the SUNCAT Center for Interface Science and Catalysis.

Author contributions

Conceptualization: X.F., V.A.N., J.K.N., T.F.J., I.C.

Data curation: X.F., V.A.N., J.B.P., S.L., K.Z., M.S., K.E.R.

Formal Analysis: X.F., V.A.N., P.B., Y.Z., K.Z., A.X., J.B.V.M., N.H.D. A.C.N.

Investigation: X.F., V.A.N., S.L., M.S.

Methodology – Equipment design: X.F., V.A.N., M.S., J.B.P., S.Z.A.

Visualization: X.F., V.A.N.

Supervision: I.C., T.F.J., J.K., P.C.K.V., J.K.N., A.C.N.

Writing – original draft: X.F., V.A.N.

Writing – review and editing: X.F., V.A.N., Y.Z., S.Z.A., A.C.N., J.K., T.F.J., I.C.

References

1. Iriawan, H. et al. Methods for nitrogen activation by reduction and oxidation. *Nat. Rev. Method Prime* **1**, 56 (2021).
2. Chen, J.G. et al. Beyond fossil fuel-driven nitrogen transformations. *Science* **360**, eaar6611 (2018).
3. Fu, X.B., Zhang, J.H. & Kang, Y.J. Recent advances and challenges of electrochemical ammonia synthesis. *Chem Catalysis* **2**, 2590-2613 (2022).
4. Survey, U. S. G., United States Geological Survey. *Mineral Commodity Summaries 2022*, 2022.
5. Erisman, J.W., Sutton, M.A., Galloway, J., Klimont, Z. & Winiwarter, W. How a century of ammonia synthesis changed the world. *Nat. Geosci.* **1**, 636-639 (2008).
6. Choi, J. et al. Identification and elimination of false positives in electrochemical nitrogen reduction studies. *Nat. Commun.* **11**, 5546 (2020).
7. Andersen, S.Z. et al. A rigorous electrochemical ammonia synthesis protocol with quantitative isotope measurements. *Nature* **570**, 504-508 (2019).
8. Greenwood, N.N., Earnshaw, E.A. Chemistry of the Elements. *Pergamon Press* (1984).
9. F. Fichter, P.G., H. Erlenmeyer Elektrolytische Bindung von komprimiertem Stickstoff bei gewöhnlicher Temperatur. *Helv. Chim. Acta* **13**, 1228–1236 (1930).
10. Tsuneto, A., Kudo, A. & Sakata, T. Efficient Electrochemical Reduction of N_2 to NH_3 Catalyzed by Lithium. *Chem. Lett.* 851-854 (1993).
11. Tsuneto, A., Kudo, A. & Sakata, T. Lithium-Mediated Electrochemical Reduction of High-Pressure N_2 to NH_3. *J. Electroanal. Chem.* **367**, 183-188 (1994).
12. Andersen, S.Z. et al. Increasing stability, efficiency, and fundamental understanding of lithium-mediated electrochemical nitrogen reduction. *Energy. Environ. Sci.* **13**, 4291-4300 (2020).
13. Cai, X.Y. et al. Lithium-mediated electrochemical nitrogen reduction: Mechanistic insights to enhance performance. *iScience* **24** (2021).
14. Lazouski, N., Chung, M.J., Williams, K., Gala, M.L. & Manthiram, K. Non-aqueous gas diffusion electrodes for rapid ammonia synthesis from nitrogen and water-splitting-derived hydrogen. *Nat. Catal.* **3**, 463-469 (2020).

15. Li, K. et al. Enhancement of lithium-mediated ammonia synthesis by addition of oxygen. *Science* **374**, 1593-1597 (2021).

16. Li, K. et al. Increasing Current Density of Li-Mediated Ammonia Synthesis with High Surface Area Copper Electrodes. *ACS Energy Lett.* **7**, 36-41 (2022).

17. McEnaney, J.M. et al. Ammonia synthesis from N_2 and H_2O using a lithium cycling electrification strategy at atmospheric pressure. *Energy. Environ. Sci.* **10**, 1621-1630 (2017).

18. Lazouski, N., Schiffer, Z.J., Williams, K. & Manthiram, K. Understanding Continuous Lithium-Mediated Electrochemical Nitrogen Reduction. *Joule* **3**, 1127-1139 (2019).

19. Suryanto, B.H.R. et al. Nitrogen reduction to ammonia at high efficiency and rates based on a phosphonium proton shuttle. *Science* **372**, 1187-1191 (2021).

20. Du, H.L. et al. Electroreduction of nitrogen with almost 100% current-to-ammonia efficiency. *Nature* **609**, 722-727 (2022).

21. Li, S. et al. Electrosynthesis of ammonia with high selectivity and high rates via engineering of the solid-electrolyte interphase. *Joule* **6**, 2083-2101 (2022).

22. Fu, X. et al. Continuous-flow electrosynthesis of ammonia by nitrogen reduction and hydrogen oxidation. *Science* **379**, 707-712 (2023).

23. Frank, A.R. On the utilisation of the atmospheric nitrogen in the production of calcium cyanamide, and its use in agriculture and chemistry. *T. Faraday. Soc.* **4**, 099-114 (1908).

24. Rosch, B. et al. Dinitrogen complexation and reduction at low-valent calcium. *Science* **371**, 1125-1128 (2021).

25. Chen, X.Y., et al. Oxygen vacancy engineering of calcium cobaltate: A nitrogen fixation electrocatalyst at ambient condition in neutral electrolyte. *Nano Res.*, **14**, 501-506 (2021).

26. Kibsgaard, J., et al. The Difficulty of Proving Electrochemical Ammonia Synthesis. *ACS Energy Lett.*, 4, 2986-2988 (2019).

27. Wang, D. et al. Plating and stripping calcium in an organic electrolyte. *Nat. Mater.* **17**, 16-20 (2018).

28. Biria, S., Pathreeker, S., Genier, F.S., Li, H.S. & Hosein, I.D. Plating and Stripping Calcium at Room Temperature in an Ionic-Liquid Electrolyte. *ACS Appl. Energy. Mater.* **3**, 2310-2314 (2020).

29. Melemed, A.M., Skiba, D.A. & Gallant, B.M. Toggling Calcium Plating Activity and Reversibility through Modulation of Ca^{2+} Speciation in Borohydride-Based Electrolytes. *J. Phys. Chem. C* **126**, 892-902 (2022).

30. Ta, K. et al. Understanding Ca Electrodeposition and Speciation Processes in Nonaqueous Electrolytes for Next-Generation Ca-Ion Batteries. *ACS Appl. Mater. Inter.* **11**, 21536-21542 (2019).

31. Ponrouch, A., Frontera, C., Barde, F. & Palacin, M.R. Towards a calcium-based rechargeable battery. *Nat. Mater*. **15**, 169-172 (2016).

32. Shyamsunder, A., Blanc, L.E., Assoud, A. & Nazar, L.F. Reversible Calcium Plating and Stripping at Room Temperature Using a Borate Salt. *ACS Energy Lett.* **4**, 2271-2276 (2019).

33. Li, Z.Y., Fuhr, O., Fichtner, M. & Zhao-Karger, Z. Towards stable and efficient electrolytes for room-temperature rechargeable calcium batteries. *Energ. Environ. Sci.* **12**, 3496-3501 (2019).

34. Nielson, K.V., Luo, J. & Liu, T.L. Optimizing Calcium Electrolytes by Solvent Manipulation for Calcium Batteries. *Batteries Supercaps* **3**, 766-772 (2020).

35. Bitenc, J. et al. Electrochemical Performance and Mechanism of Calcium Metal-Organic Battery. *Batteries Supercaps* **4**, 214-220 (2021).

36. McShane E J. et al. A Versatile $Li_{0.5}FePO_4$ Reference Electrode for Nonaqueous Electrochemical Conversion Technologies. *ACS Energy Lett*. **8**, 230-235 (20221).

37. Vandoveren, H. & Verhoeven, J.A.T. Xps Spectra of Ca, Sr, Ba and Their Oxides. *J. Electron Spectrosc.* **21**, 265-273 (1980).

38. Su, Y.G., Huang, S.S., Wang, T.T., Peng, L.M. & Wang, X.J. Defect-meditated efficient catalytic activity toward p-nitrophenol reduction: A case study of nitrogen doped calcium niobate system. *J. Hazard Mater.* **295**, 119-126 (2015).

39. Gao, W., Guo, J., Wang, P. et al. Production of ammonia via a chemical looping process based on metal imides as nitrogen carriers. *Nat. Energy* **3**, 1067-1075 (2018).

40. Wietelmann, U., Felderhoff, M. and Rittmeyer, P. (2016). Hydrides. *Ullmann's Encyclopedia of Industrial Chemistry*, pp 10-11.

41. Il'inchik, E.A., Volkov, V.V. & Mazalov, L.N. X-ray photoelectron spectroscopy of boron compounds. *J. Struct. Chem.* **46**, 523-534 (2005).

42. Prabakar, S.J.R., et al. Graphite as a Long-Life Ca^{2+}-Intercalation Anode and its Implementation for Rocking-Chair Type Calcium-Ion Batteries. *Adv. Sci.*, **6**, 1902129 (2019).
43. Park, J., et al. Stable and High-Power Calcium-Ion Batteries Enabled by Calcium Intercalation into Graphite. *Adv. Mater.*, **32**, 1904411 (2020).

Supplementary Material

X-ray chemical imaging for assessing redox microsites within soils and sediments

Vincent Noël[a,*], Kristin Boye[a], Hannah Naughton[b,c], Emily Lacroix[d,e], Meret Aeppli[d,f], Naresh Kumar[g], Scott Fendorf[d], and Samuel M. Webb[a]

[a] *Stanford Synchrotron Radiation Lightsource, SLAC National Accelerator Laboratory, 2575 Sand Hill Road, Menlo Park, CA 94025, USA*

[b] *Climate and Ecosystem Sciences Division at Lawrence Berkeley National Laboratory, 1 Cyclotron Rd, Berkeley, CA 94720*

[c] *Stockbridge school of Agriculture, University of Massachusetts, Amherst, MA 01003, USA*

[d] *Department of Earth System Science, Stanford University, Stanford, CA 94305, USA*

[e] *Institut des Dynamiques de la Surface Terrestre (IDYST), Université de Lausanne, 1015 Lausanne, Switzerland*

[f] *Institut d'ingénierie de l'environnement (IIE), École Polytechnique Fédérale de Lausanne, 1015 Lausanne, Switzerland*

[g] *Soil Chemistry, Wageningen University and Research, PO Box 47, 6700AA Wageningen, The Netherlands*

submitted to

Frontiers in Environmental Chemistry

Special Issue: Advanced Techniques for the Chemical Imaging of Metals in Environmental Sciences

*Corresponding author: Vincent Noël; e-mail: noel@slac.stanford.edu

1) Verification of mineral phase purity composing the synthetic cores

2) Example of analysis of full Fe K-edge µ-XANES spectra across multiple putative redox anomalies

3) Selection of the energy positions for the Fe K-edge multiple energy µ-XRF mapping

4) Identification of Fe components using SiVM fitting

5) Excluding false positive redox microsites based on comparisons of the same Fe component obtained from XANES and SiVM fitting

6) Excluding false positive redox microsites based on comparisons of distinct Fe components

1) Verification of mineral phase purity composing the synthetic cores

X-ray diffraction procedure and results. Phase purity of the synthetic goethite, composing the Fe^{III}-(hydroxy)oxides microsite, natural Fe^{II}-Sulfide (i.e., pyrite and residues of FeS) composing the Fe^{II}-S microsite, and natural siderite composing the $Fe^{II}CO_3$ microsite, were confirmed by X-ray diffraction (XRD) analysis using a Rigaku MiniFlex 600 Benchtop X-ray Diffraction System at the Cu wavelength (λ=1.5406 Å) and phase identification was performed by automatic search, using the Inorganic Crystal Structure Database (ICSD, ©2019 FIZ Karlsruhe GmbH).

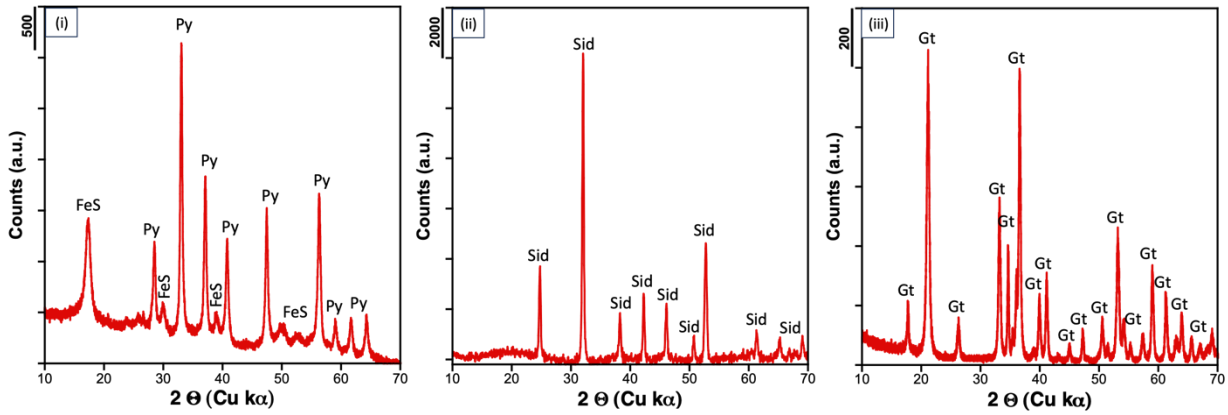

Figure SM-1. *X-ray diffractogram of: (i) natural Fe^{II}-sulfide, (ii) natural siderite (=Sid), and (iii) synthetic goethite (=Gt). Iron sulfide is composed of a mix of pyrite (=Py) and FeS.*

2) Example of analysis of full Fe K-edge μ-XANES spectra across multiple putative redox anomalies

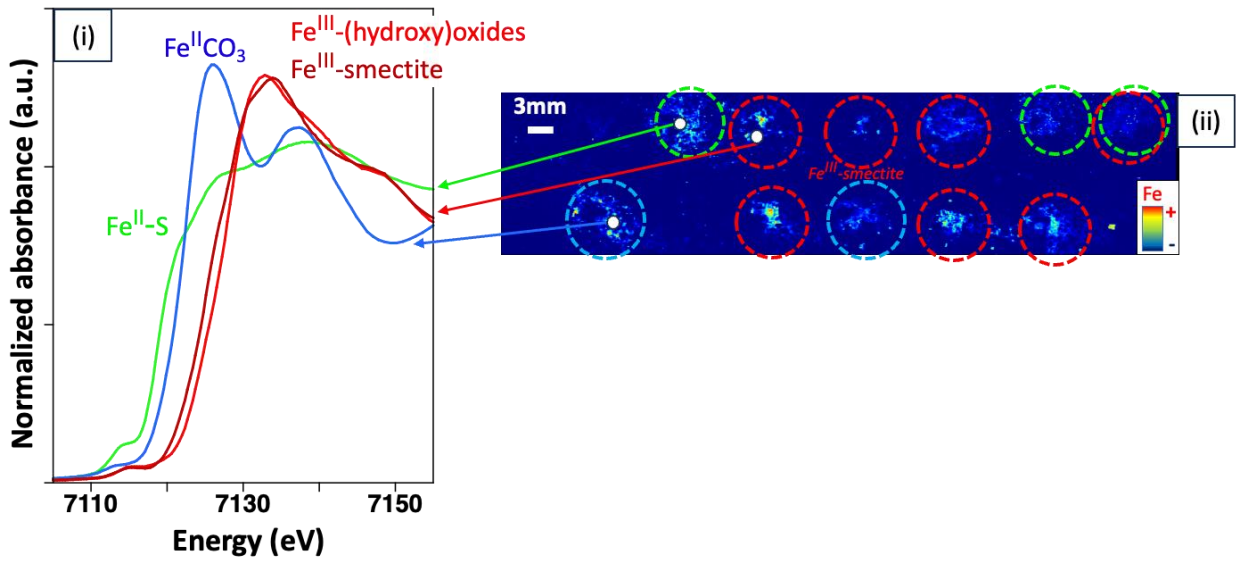

Figure SM-2. *(i) Full Fe K-edge μ-XANES spectra collected from (ii) the map of putative redox anomalies highlighted by SiVM fitting of multi-energy Fe K-edge μ-XRF maps of Fe^{II}-S, $Fe^{II}CO_3$, and Fe^{III}-(hydroxy)oxides microsites in the Fe^{III}-free sand synthetic core. The white circles show the analysis location of full Fe K-edge μ-XANES spectra. The real locations of Fe^{II}-S, $Fe^{II}CO_3$, and Fe^{III}-(hydroxy)oxide microsites are marked with green, blue, and red dashed circles, respectively.*

3) Selection of the energy positions for the Fe K-edge multiple energy μ-XRF mapping

The energy position of the Fe *K*-edge XANES spectrum mainly depends on the redox state of Fe in Fe-bearing minerals.

The Fe 3d pre-edge of Fe^0 (metallic Fe) is centered around 7114 -7116 eV (Westre *et al.*, 1997; **Figure SM-3a**). Contrary to Fe^{II} and Fe^{III} pre-edge, the Fe 3d pre-edge of Fe^0 is characterized by significant high intensity of absorbed X-ray energy (~ 0.5 in normalized absorbance), thus energy corresponding to the Fe 3d pre-edge of Fe^0 can be reliably selected to detect the presence of Fe^0 species. Although the actual number and positions of absorption features in the pre-edge region of Fe *K*-edge XANES spectra depends on the symmetry and distortion of the site, it is considered that Fe^{III} is characterized by absorption features centered around 7114 eV, whereas Fe^{II} is characterized by absorption features centered around 7112 eV (Wilke *et al.*, 2001;

Galoisy *et al.*, 2001; Farges *et al.*, 2004). Thus, 7116 eV was selected for μ-XRF mapping in order to contrast the presence of Fe^{0} species with Fe^{II}- and Fe^{III}-species.

The energy of the white-line of the XANES spectra of the Fe-S species is typically in the range of 7120-7123 eV, while other Fe^{II}-species are typically in the range between 7125-7129 eV with an average of 7127 eV (**Figure SM-3a**). Thus, 7123 eV and 7127 eV were both selected for μ-XRF mapping to contrast the presence of Fe-S species (Fe^{II}-S and $Fe^{II/III}$-S, *i.e.* greigite) with other Fe^{II}-species, respectively. 7127 eV corresponds also to the white-line of the XANES spectra of some $Fe^{II/III}$-silicate references (**Figure SM-3b**), however, because the intensity of the absorbed energy decreases above 7127 eV for Fe^{II}-species while increases for $Fe^{II/III}$-silicate references up to 7131-7132 eV, the difference of the intensity of absorbed X-ray energy between 7127 eV and 7132 eV should provide enough information to contrast the presence of Fe^{II}-species *vs* $Fe^{II/III}$-silicate.

The energy of the white-line of the XANES spectra of the Fe-(hydroxy)oxides and Fe^{III}-species are typically in the range of 7131-7138 eV (**Figure SM-3c**). The energy 7132 eV captures $Fe^{II/III}$-(hydroxy)oxides and Fe^{III}-(hydroxy)oxides, so, 7132 eV was selected for μ-XRF mapping to detect the presence of both $Fe^{II/III}$- and Fe^{III}- (hydroxy)oxides. However, as we previously underlined, 7132 eV corresponds also to the white-line of the XANES spectra of a large set of $Fe^{II/III}$-silicate references (**Figure SM-3b**). Thus, in addition, 7138 eV was also selected for μ-XRF mapping to contrast the presence of Fe^{III}- (hydroxy)oxides while excluding a majority of $Fe^{II/III}$-silicate references (**Figure SM-3b**), even if some reference compounds of Fe^{III}-clays, such as Fe^{III}-smectite, cannot be distinguished from Fe^{III}-(hydroxy)oxides (**Figure 4**) with this approach. An alternative to collecting less maps, would be to obtain a μ-XRF map at 7134 eV instead of 7132 eV and 7138 eV, which is sensitive to Fe^{III}-O species.

Finally, because the intensity of the absorbed energy decreases above 7138 eV for all Fe-species (mainly for Fe^{III}-species), an additional energy above 7138 eV has been randomly selected to represent the post-edge (*i.e.*, 7145 eV). Thus, the set of Fe intensities for each incident energy results in a shortened spectrum of Fe fluorescence intensity as a function of energy, similar to a XANES spectrum where 7145 eV corresponds to the post-edge. Furthermore, the Fe fluorescence peak intensity at the post-edge incident energy (*i.e.*, 7145 eV) corresponds also to the total Fe fluorescence intensity.

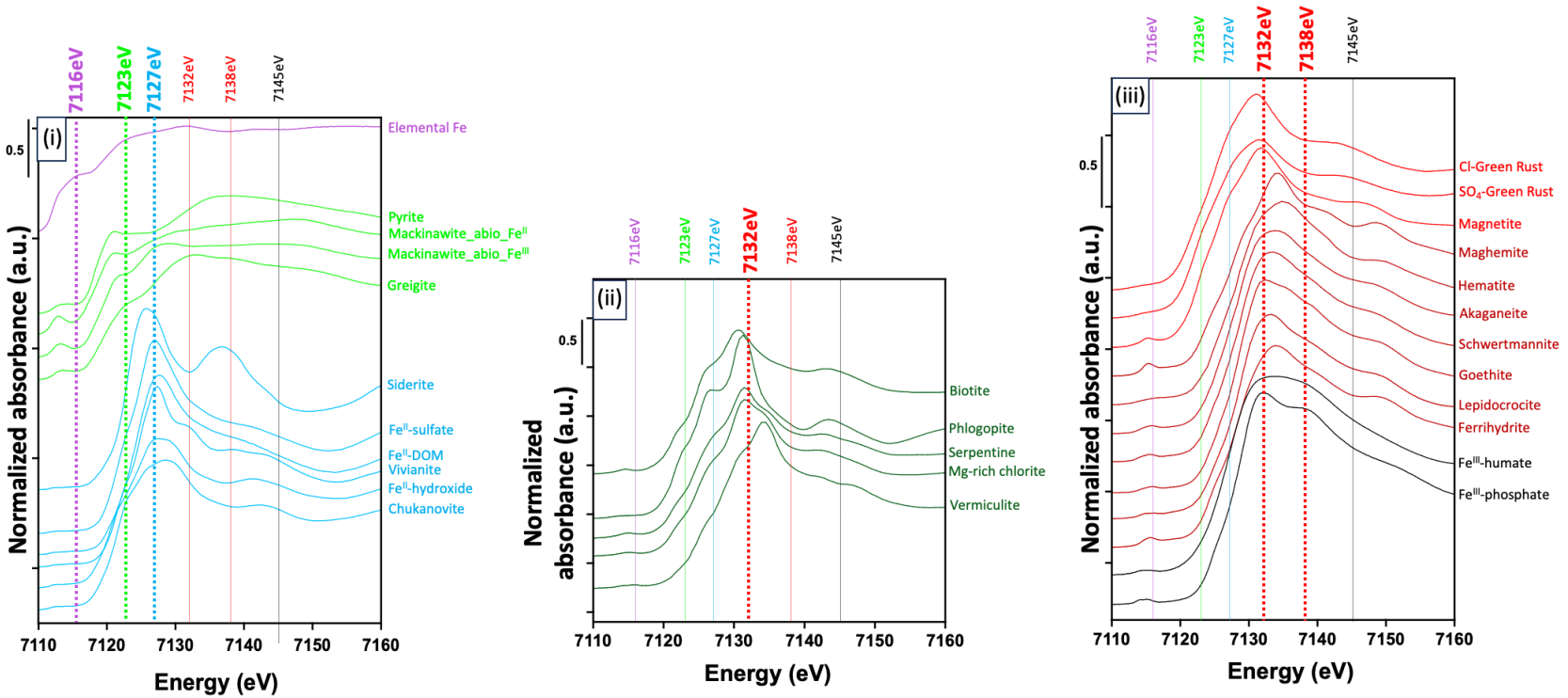

Figure SM-3. *Fe K-edge XANES spectra of reference compounds representative of the most commonly found Fe species in both oxic and anoxic soils to give the highest contrast between oxidation/chemical states. The large set of XANES spectra is displayed respectively in three groups: (i) Fe^{0}, Fe-S species and Fe^{II}-species; (ii) $Fe^{II/III}$-silicates; and (iii) Fe-(hydroxy)oxides and Fe^{III}-species. The dashed purple, green, blue, and red lines indicate the energy selected for each μ-XRF map for capturing Fe^{0}, Fe-S species, other Fe^{II}-species, and $Fe^{II/III}$-(hydroxy)oxides, respectively. The black dashed lines indicate the energy selected for capturing the post-edge. The chemical formula, the source, and the reference of each compound are provided in* ***Table SM-1****.*

Table SM-1: *Iron reference compounds analyzed by XANES.*

Compound	Chemical formula	Source/synthesis	Reference
Elemental Fe	Fe^0	Metallic foil	EXAFS material, 2023
Pyrite	FeS_2 [a,b]	Synthetic	Morin *et al.*, 2017
Mackinawite_abio_Fe^{II}	FeS[a,b]	Synthesized with Fe^{II}	Bone *et al.*, 2014
Mackinawite_abio_Fe^{III}	FeS [a,b]	Synthesized with abiotic reduction of Fe^{III}	Morin *et al.*, 2017
Greigite	Fe_3S_4 [a,b]	Synthetic	Noël *et al.*, 2014
Siderite	$Fe(CO_3)$ [a,b]	Synthetic	Dublet *et al.*, 2012
Fe^{II}-sulfate heptahydrate	$FeSO_4 \cdot 7H_2O$ [a,b]	Sigma	Kumar *et al.*, 2018
Fe^{II}-DOM DOM=Suwannee River Fulvic Acid (SRFA)	Not determined	Synthetic	Trusiak *et al.*, 2018
Vivianite	$Fe_3(PO_4)_2 \cdot 8H_2O$ [a,b]	Synthetic	Cosmidis *et al.*, 2014
Fe^{II}-hydroxide	$Fe(OH)_2$ [a,b]	Synthetic	Ona-Nguema *et al.*, 2009
Chukanovite	$Fe_2(CO_3)(OH)_2$ [a,b]	Synthetic	Azoulay *et al.*, 2012
Biotite	Not determined	Natural, Mineralogy Collection of IMPMC, Paris, France	Othmane *et al.*, 2013
Phlogopite	Not determined	Natural	Mineral collection, IMPMC, Paris VI, France
Serpentine	Not determined	Natural, New Idria Mining District (CA, USA)	Noël *et al.*, 2014
Mg-rich chlorite	Not determined	Natural, by D. Beaufort, Université de Poitiers, France	Othmane *et al.*, 2013
Vermiculite	Not determined	Natural	Mineral collection, IMPMC, Paris VI, France
Cl-Green Rust	Not determined	Synthetic	LBL database
SO_4-Green Rust	Not determined	Synthetic	LBL database, Pantke *et al.*, 2012
Magnetite	Fe_3O_4 [a,b]	Synthetic (biogenic)	Wang *et al.*, 2008
Maghemite	χ-Fe_2O_3 [a,b]	Synthetic	Hohmann *et al.*, 2011
Hematite	α-Fe_2O_3 [a,b]	Synthetic	Hohmann *et al.*, 2011
Akaganeite	β-FeOOH[a,b]	Synthetic	Hohmann *et al.*, 2011
Schwertmannite	$Fe_8O_8(OH)_6SO_4$ [a,b]	Synthetic	Maillot *et al.*, 2013
Goethite	α-FeOOH[a,b]	Synthetic	Maillot *et al.*, 2011
Lepidocrocite	χ-FeOOH[a,b]	Synthetic	Ona-Nguema *et al.*, 2005
Ferrihydrite (6-line)	$Fe^{III}_2O_3 \cdot 0.5H_2O$ [a,b]	Synthetic	Maillot *et al.*, 2011
Fe^{III}-humate (solid OM)	Not determined	Purified colloidal material from Rio Negro River (Brazil)	Allard *et al.*, 2011 Cosmidis *et al.*, 2014
Fe^{III}-phosphate	$FePO_4$ [a,b]	Natural	Cosmidis *et al.*, 2014

[a]*estimated by X-ray Absorption Spectroscopy*

[b]*X-ray diffraction confirmed*

4) Identification of Fe components using SiVM fitting

In this section, the map of the contribution spatial distribution of each Fe component of SiVM fitting in Fe^{III}-free sand and Fe^{III}-smectite sand environments is compared with the map of the contribution spatial distribution of the Fe^{II}-S, $Fe^{II}CO_3$, and Fe^{III}–(hydroxy)oxide components of XANES fitting to determine to which Fe component each SiVM fitting component map is most similar to.

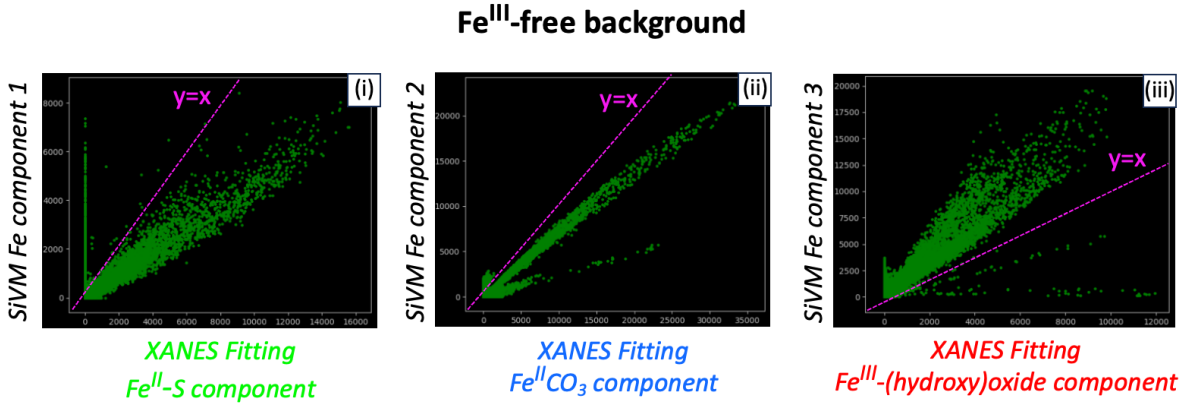

Figure SM-4. *Retained correlation plots of Fe components' contribution of SiVM fitting (y -axes) compared with the contribution of the (i) Fe^{II}-S, (ii) $Fe^{II}CO_3$, and (iii) Fe^{III}-(hydroxy)oxides components of XANES fitting (x -axes) in each pixel of multiple Fe K-edge μ-XRF maps of Fe^{II}-S, $Fe^{II}CO_3$, and Fe^{III}-(hydroxy)oxides microsites in the Fe^{III}-free sand synthetic core. The contribution of each Fe component, regardless the fitting method (x- and y-axes), is expressed as the proportion of total Fe counts. The dashed purple lines indicate an ideal spatial distribution y=x, i.e. a slope of 1, between the two fitting methods.*

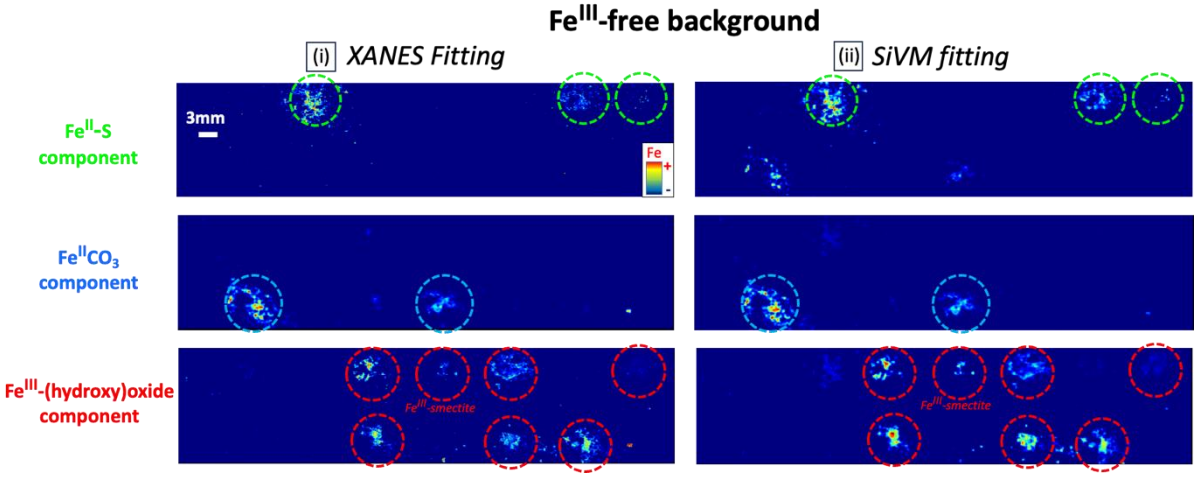

Figure SM-5. *Initial (without refinement of data processing) maps of the spatial distribution of the contribution of Fe^{II}-S (top), $Fe^{II}CO_3$ (middle), and Fe^{III}-(hydroxy)oxide (bottom) components of (i) XANES and (ii) SiVM fittings of multi-energy Fe K-edge μ-XRF maps of Fe^{II}-S, $Fe^{II}CO_3$, and Fe^{III}-(hydroxy)oxides microsites in the Fe^{III}-free sand synthetic core. The real locations of Fe^{II}-S, $Fe^{II}CO_3$, and Fe^{III}-(hydroxy)oxide microsites are marked with green, blue, and red dashed*

*circles, respectively. A Fe^{III}-smectite microsite was also added, as indicated in the bottom panels. Due to the spectral similarities (in energy and intensity) of the Fe^{III}-smectite XANES spectrum and the Fe^{III}-(hydroxy)oxide XANES spectrum (**Figure SM-2**), the Fe^{III}-smectite microsite is included in the Fe^{III}-(hydroxy)oxide component.*

Figure SM.6 *Retained correlation plots of Fe components' contribution of SiVM fitting (y -axes) compared with the contribution of the (i) Fe^{II}-S, (ii) $Fe^{II}CO_3$, and (iii) Fe^{III}-(hydroxy)oxides components of XANES fitting (x -axes) in each pixel of multiple Fe K-edge μ-XRF maps of Fe^{II}-S, $Fe^{II}CO_3$, and Fe^{III}-(hydroxy)oxides microsites in the Fe^{III}-smectite sand synthetic core. The contribution of each Fe component, regardless the fitting method (x- and y-axes), is expressed as the proportion of total Fe counts. The dashed purple lines indicate an ideal spatial distribution y=x, i.e. a slope of 1, between the two fitting methods.*

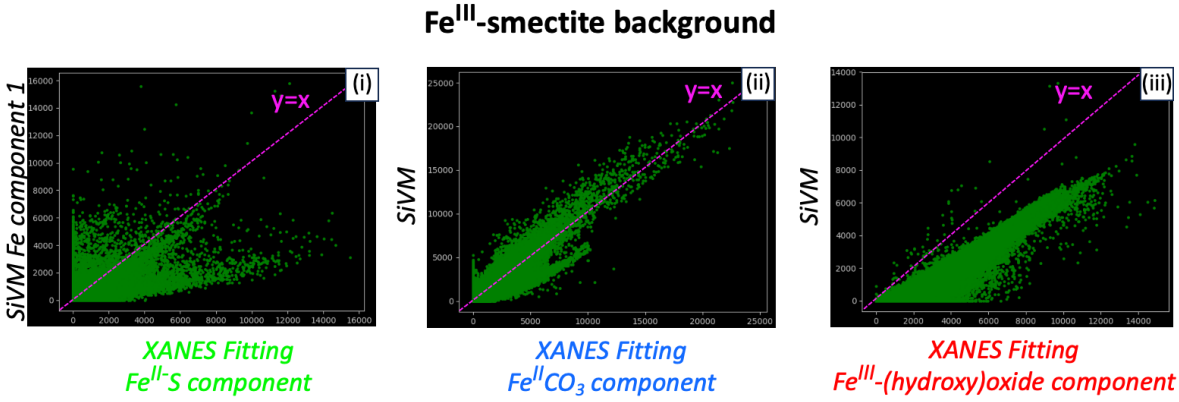

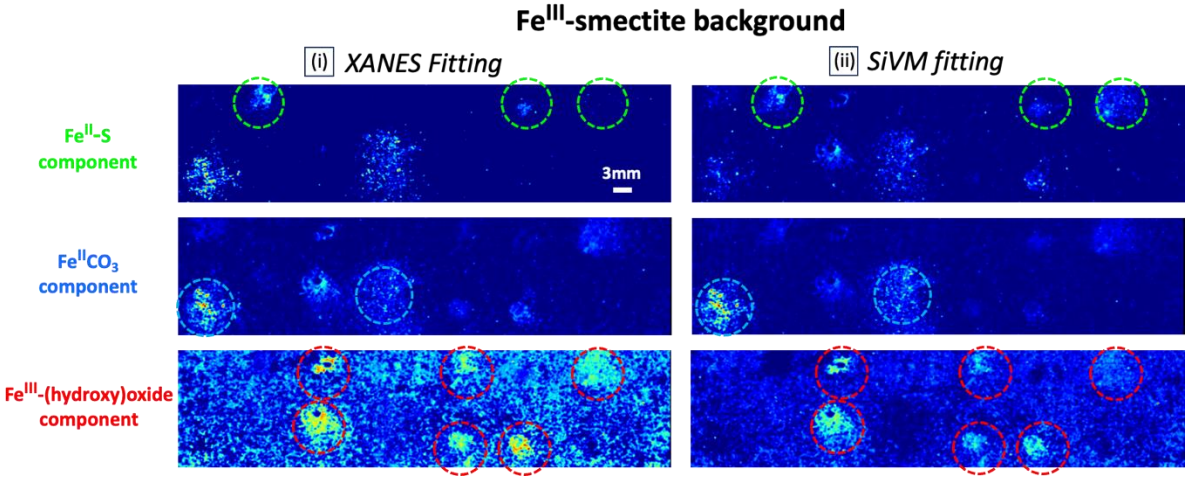

Figure SM-7. *Initial (without refinement of data processing) maps of the spatial distribution of the contribution of Fe^{II}-S (top), $Fe^{II}CO_3$ (middle), and Fe^{III}-(hydroxy)oxide (bottom) components of (i) XANES and (ii) SiVM fittings of multi-energy Fe K-edge μ-XRF maps of Fe^{II}-S, $Fe^{II}CO_3$, and Fe^{III}-(hydroxy)oxides microsites in the Fe^{III}-smectite sand synthetic core. The real locations of Fe^{II}-S, $Fe^{II}CO_3$, and Fe^{III}-(hydroxy)oxide microsites are marked with green, blue, and red dashed circles, respectively.*

5) Excluding false positive redox microsites based on comparisons of the same Fe component obtained from XANES and SiVM fitting

In this section, we re-mapped each of the $Fe^{II}S_2$, $Fe^{II}CO_3$, and Fe^{III}-(hydroxy)oxide components based on comparing the contribution spatial distribution of the same Fe component obtained from the two distinct fitting methods, *i.e.* XANES and SiVM.

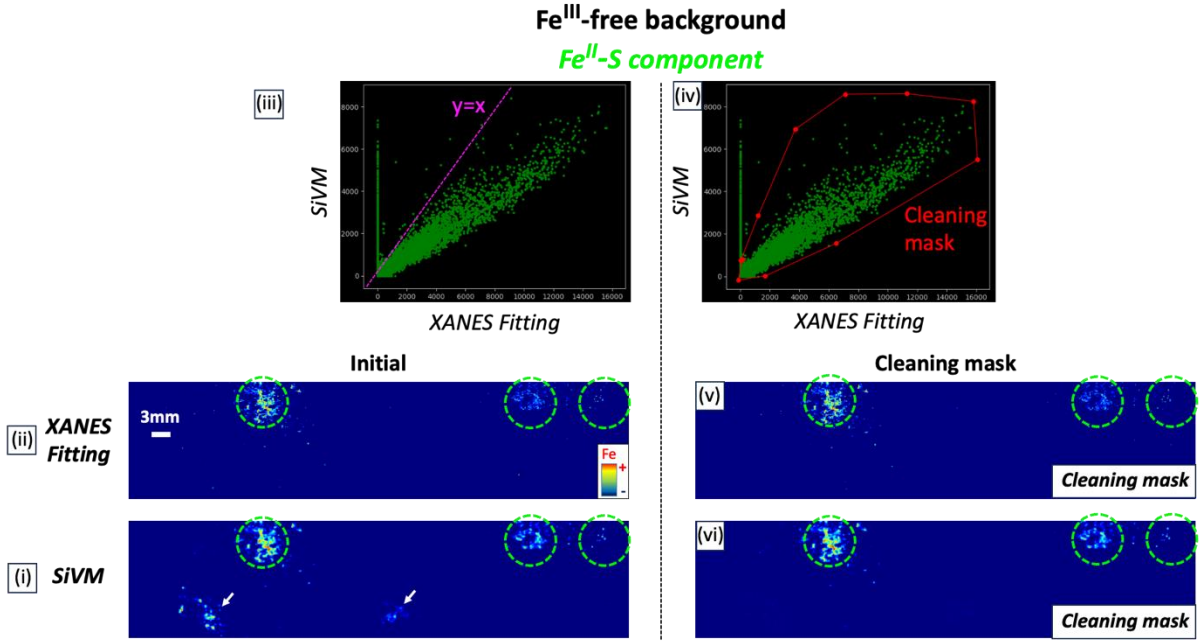

Figure SM-8. Left: *Initial (without refinement of data processing) map of the spatial distribution of the Fe^{II}-S component contribution of (i) SiVM fitting and (ii) XANES fitting. White arrows indicate the false positives in the Fe^{II}-S component spatial distribution of XANES fitting compared to the SiVM fitting; (iii) Correlation plot of the contribution of the Fe^{II}-S component of XANES fitting with SiVM fitting in each pixel of Fe K-edge multiple energy μ-XRF maps of Fe^{II}-S, $Fe^{II}CO_3$, and Fe^{III}-(hydroxy)oxide microsites in the Fe^{III}-free sand synthetic core. The contribution of Fe component, regardless the fitting method (x- and y-axes), is expressed as the proportion of total Fe counts. The dashed purple line (top left panel) indicates an ideal spatial distribution y=x, i.e. a slope of 1, between the two fitting methods.*

Right: *(i) Mask (outlined in red) defined to select points (i.e., pixels) from the correlation plot to re-map the contribution spatial distribution of the Fe^{II}-S component from the XANES and SiVM fittings. Points excluded in the masking process are not linearly and simultaneously present in both the XANES and SiVM fitting maps; Re-mapping of the spatial distribution of the Fe^{II}-S component contribution of (v) XANES fitting and (vi) SiVM fitting.*

Note: *The false positive Fe^{II}-S microsites indicated by white arrows in (i) were successively removed in reconstructed maps (v and vi) after re-mapping the Fe^{II}-S component using exclusively the correlated points between XANES and SiVM fitting (i.e., the 'cleaning mask'). The real locations of the Fe^{II}-S microsites are marked with green dashed circles.*

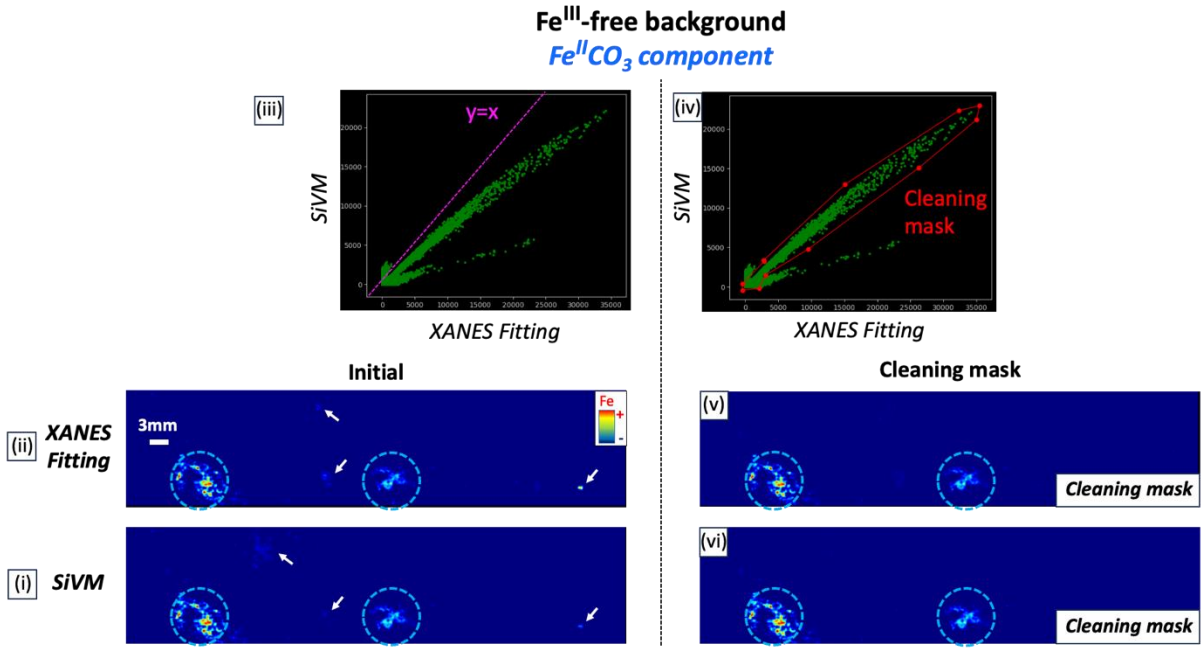

Figure SM-9. Left: *Initial (without refinement of data processing) map of the spatial distribution of the $Fe^{II}CO_3$ component contribution of (i) SiVM fitting and (ii) XANES fitting. White arrows indicate the false positives in the $Fe^{II}CO_3$ component spatial distribution of XANES fitting compared to the SiVM fitting; (iii) Correlation plot of the contribution of the $Fe^{II}CO_3$ component of XANES fitting with SiVM fitting in each pixel of Fe K-edge multiple energy μ-XRF maps of Fe^{II}-S, $Fe^{II}CO_3$, and Fe^{III}-(hydroxy)oxide microsites in the Fe^{III}-free sand synthetic core. The contribution of Fe component, regardless the fitting method (x- and y-axes), is expressed as the proportion of total Fe counts. The dashed purple line (top left panel) indicates an ideal spatial distribution y=x, i.e. a slope of 1, between the two fitting methods.*

Right: *(i) Mask (outlined in red) defined to select points (i.e., pixels) from the correlation plot to re-map the contribution spatial distribution of the $Fe^{II}CO_3$ component from the XANES and SiVM fittings. Points excluded in the masking process are not linearly and simultaneously present in both the XANES and SiVM fitting maps; Re-mapping of the spatial distribution of the $Fe^{II}CO_3$ component contribution of (v) XANES fitting and (vi) SiVM fitting.*

Note: *The false positive $Fe^{II}CO_3$ microsites indicated by white arrows in (i) and (ii) were successively removed in reconstructed maps (v and vi) after re-mapping the $Fe^{II}CO_3$ component using exclusively the correlated points between XANES and SiVM fitting (i.e., the 'cleaning mask'). The real locations of the $Fe^{II}CO_3$ microsites are marked with blue dashed circles.*

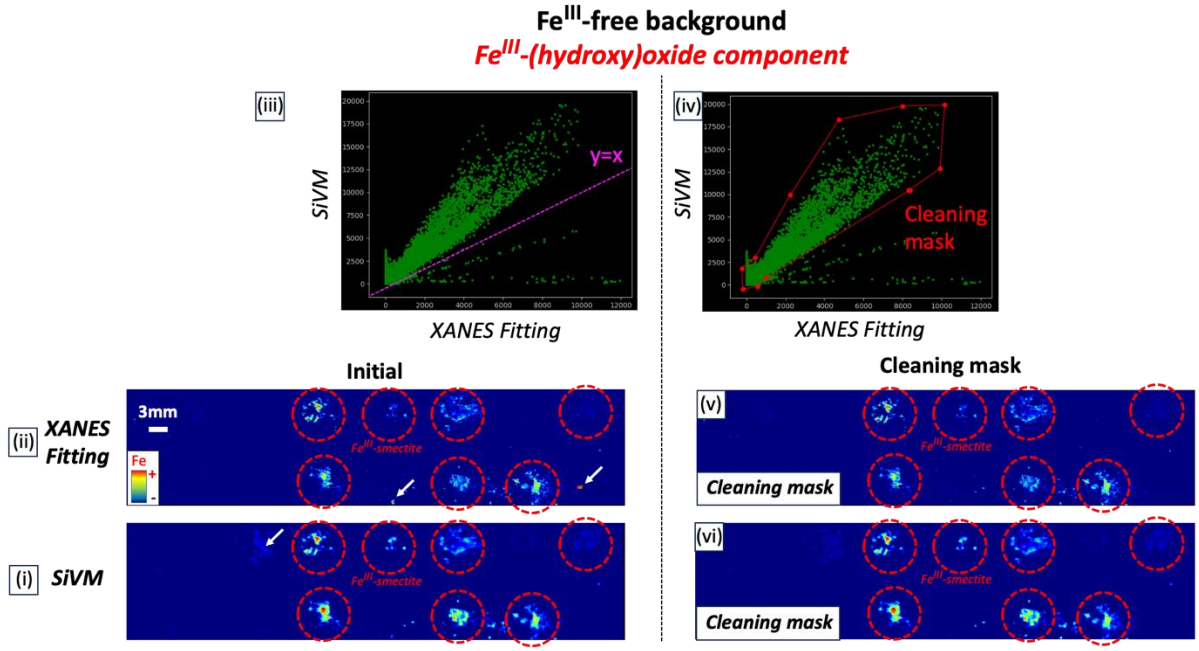

Figure SM-10. Left: *Initial (without refinement of data processing) map of the spatial distribution of the Fe^{III}-(hydroxy)oxide component contribution of (i) SiVM fitting and (ii) XANES fitting. White arrows indicate the false positives in the Fe^{III}-(hydroxy)oxide component spatial distribution of XANES fitting compared to the SiVM fitting; (iii) Correlation plot of the contribution of the Fe^{III}-(hydroxy)oxide component of XANES fitting with SiVM fitting in each pixel of Fe K-edge multiple energy μ-XRF maps of Fe^{II}-S, Fe^{II}CO$_3$, and Fe^{III}-(hydroxy)oxide microsites in the Fe^{III}-free sand synthetic core. The contribution of Fe component, regardless the fitting method (x- and y-axes), is expressed as the proportion of total Fe counts. The dashed purple line (top left panel) indicates an ideal spatial distribution y=x, i.e. a slope of 1, between the two fitting methods.*

Right: *(i) Mask (outlined in red) defined to select points (i.e., pixels) from the correlation plot to re-map the contribution spatial distribution of the Fe^{III}-(hydroxy)oxide component from the XANES and SiVM fittings. Points excluded in the masking process are not linearly and simultaneously present in both the XANES and SiVM fitting maps; Re-mapping of the spatial distribution of the Fe^{III}-(hydroxy)oxide component contribution of (v) XANES fitting and (vi) SiVM fitting.*

Note: *The false positive Fe^{III}-(hydroxy)oxide microsites indicated by white arrows in (i) and (ii) were successively removed in reconstructed maps (v and vi) after re-mapping the Fe^{III}-(hydroxy)oxide component using exclusively the correlated points between XANES and SiVM fitting (i.e., the 'cleaning mask'). The real locations of Fe^{III}-(hydroxy)oxide microsites are marked with red dashed circles.*

6) Excluding false positive redox microsites based on comparisons of distinct Fe component

Theoretically, if the contribution of each Fe component was properly differentiated in each pixel, no correlation should be observed while comparing with the contribution a distinct Fe component, regardless of the fitting method. In this section, we re-mapped each Fe^{II}-S, Fe^{II}CO$_3$, and Fe^{III}-(hydroxy)oxide component map based on comparing the contribution spatial distribution

of two distinct Fe components, obtained either from XANES and/or SiVM fitting. Using Fe component maps generated from both fitting methodologies improves the statistic comparison.

Some comparisons were not conclusive and did not show any correlation curve (**Figure SM-11**). Others, that showed correlation curve(s), were further selected for refining map of the contribution spatial distribution of each Fe component (**Figure SM-12 and SM-13**). The cloud of points (i.e., pixels) distributed along correlation curve(s) were selected for re-mapping the Fe component of XANES or SiVM fitting plotted along the axis the closest from the correlation curve(s). For example, if the slope of correlation curve(s) was below 1, the cloud of points (*i.e.*, pixels) that is near the correlation curve(s), including points below the curve(s), were attributed to the component plotted in x-axis and thus selected in a 'Mask' to re-map this component (**Figure SM-13**). The rest of the points were selected to re-map the component plotted in y-axis. Fe^{II}-S, $Fe^{II}CO_3$, and Fe^{III}–(hydroxy)oxide components can be re-mapped multiple times following different paths. Thus, the contribution of each re-mapped Fe^{II}-S component can be compared together in each pixel *via* correlation plot (**Figure SM-14**), and similarly for $Fe^{II}CO_3$, (**Figure SM-15**) and Fe^{III}–(hydroxy)oxide (**Figure SM-16**) components. Finally, the correlation curve describing the contribution spatial distribution of the same Fe component obtained from 2 different paths of re-mapping was selected for a second re-mapping for removing the last false positives (**Figure SM-14, SM-15, and SM-16**).

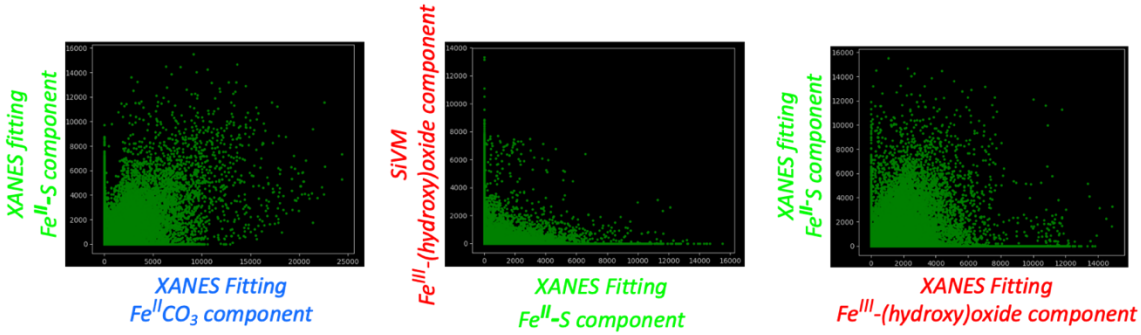

Figure SM-11. *Example of correlation plot not conclusive of the contribution of two distinct Fe components, obtained from either XANES and/or SiVM fitting, in each pixel of Fe K-edge multiple energy μ-XRF maps of Fe^{II}-S, $Fe^{II}CO_3$, and Fe^{III}-(hydroxy)oxide microsites in the Fe^{III}-smectite sand synthetic core.*

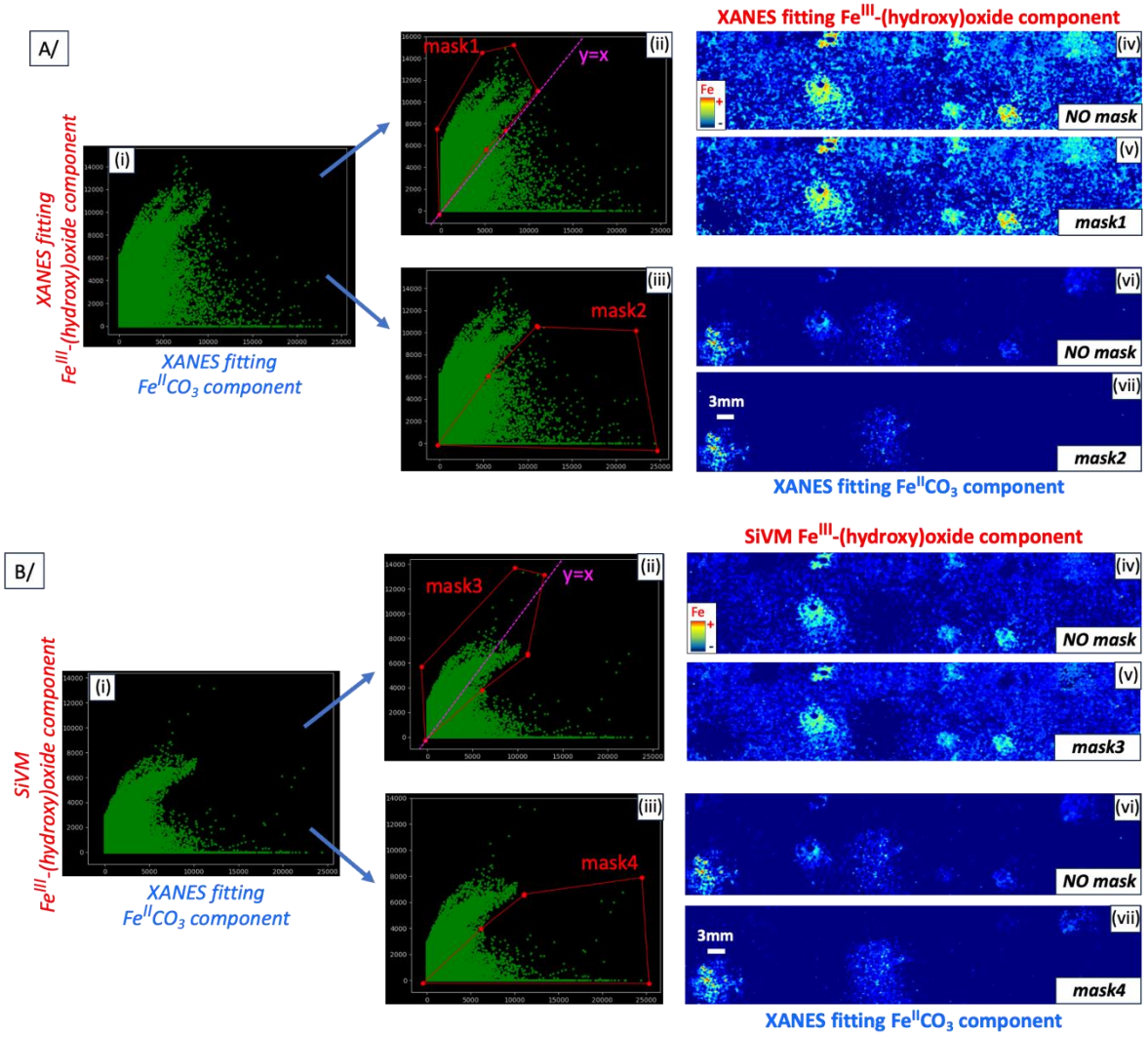

Figure SM-12 A, and B. First re-mapping based on comparing of distinct Fe component.
(i) Correlation plot of the contribution of two distinct Fe components, obtained from either XANES and/or SiVM fitting, in each pixel of Fe K-edge multiple energy μ-XRF maps of Fe^{II}-S, $Fe^{II}CO_3$, and Fe^{III}-(hydroxy)oxide microsites in the Fe^{III}-smectite sand synthetic core; (ii) The correlation curve(s) between both components being above the correlation curve(s) showing an ideal distribution y=x (i.e. slope of 1 in the dashed purple line), the cloud of points (i.e., pixels) near the correlation curve(s), including point above the curve(s), are selected to re-map component plotted in y-axis (i.e., the mask 1 and 3); (iii) The rest of the point are selected to re-map component plotted in x-axis (i.e., the mask 2 and 4); Comparison of the contribution spatial distribution map of the Fe components plotted in y-axis (iv) before and (v) after re-mapping using exclusively the points composing the mask in (ii). Comparison of the contribution spatial distribution map of the Fe components plotted in x-axis (vi) before and (vii) after re-mapping, using exclusively the points composing the mask in (iii).

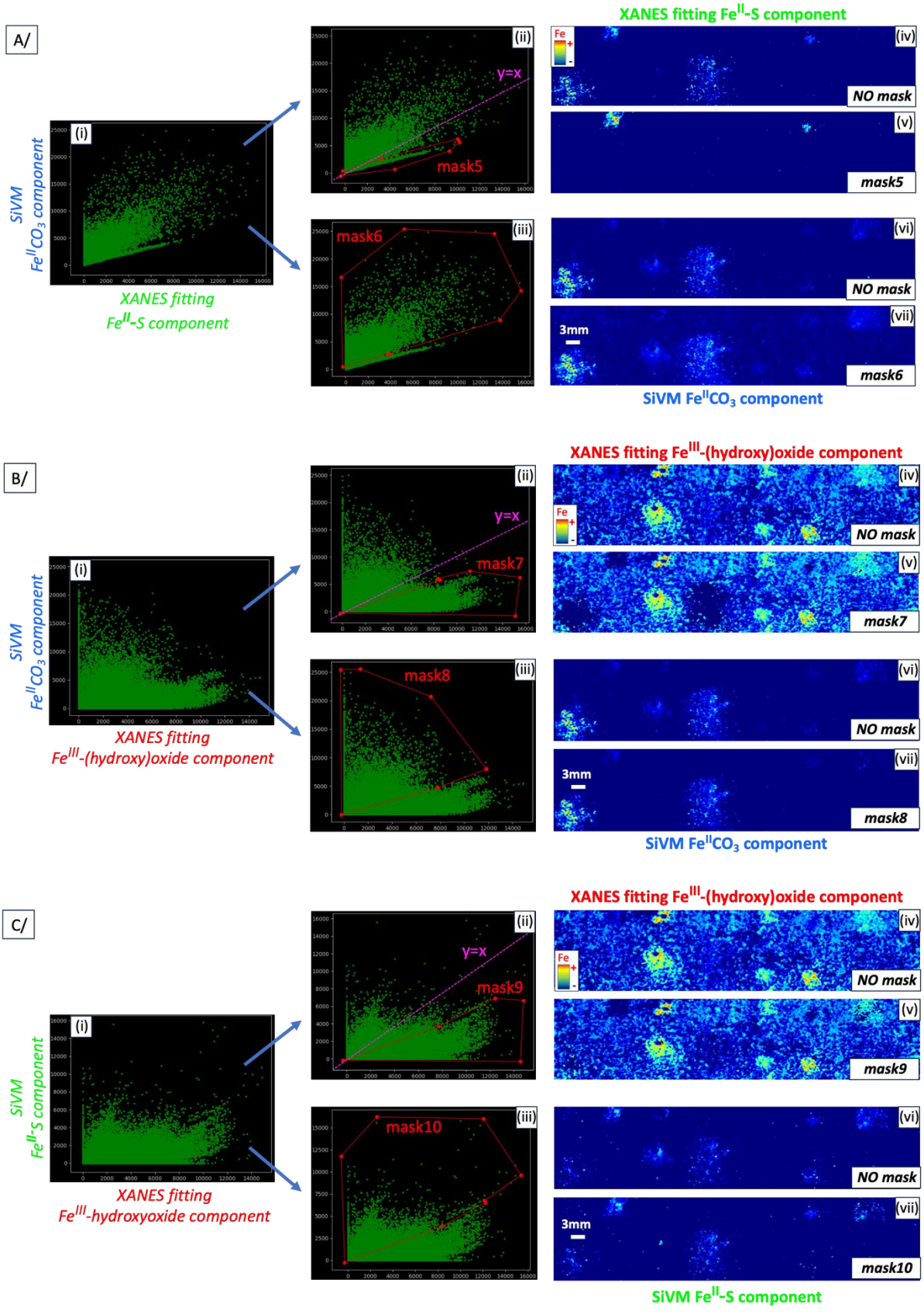
A/
SiVM Fe^{II}CO$_3$ component
(i)
XANES fitting Fe^{II}-S component
(ii)
y=x
mask5
mask6
(iii)
XANES fitting Fe^{II}-S component
Fe
(iv)
NO mask
(v)
mask5
(vi)
NO mask
3mm
(vii)
mask6
SiVM Fe^{II}CO$_3$ component
B/
SiVM Fe^{II}CO$_3$ component
(i)
XANES fitting Fe^{III}-(hydroxy)oxide component
(ii)
y=x
mask7
mask8
(iii)
XANES fitting Fe^{III}-(hydroxy)oxide component
Fe
(iv)
NO mask
(v)
mask7
(vi)
NO mask
3mm
(vii)
mask8
SiVM Fe^{II}CO$_3$ component
C/
SiVM Fe^{II}-S component
(i)
XANES fitting Fe^{III}-hydroxyoxide component
(ii)
y=x
mask9
mask10
(iii)
XANES fitting Fe^{III}-(hydroxy)oxide component
Fe
(iv)
NO mask
(v)
mask9
(vi)
NO mask
3mm
(vii)
mask10
SiVM Fe^{II}-S component

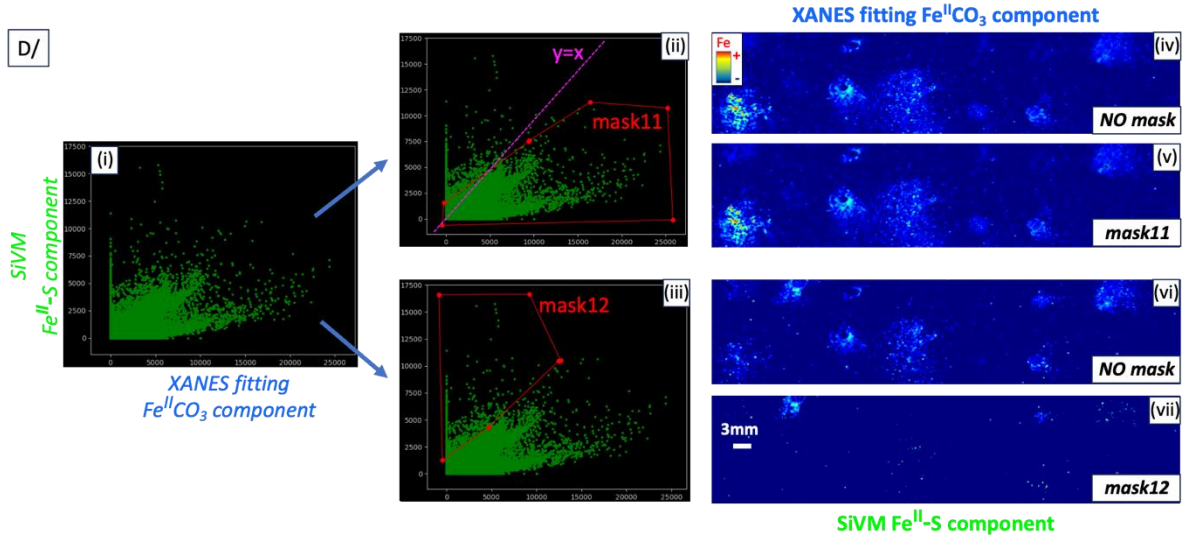

Figure SM-13 A, B, C, and D. First re-mapping based on comparison of distinct Fe component. *(i) Correlation plot of the contribution of two distinct Fe components, obtained from either XANES and/or SiVM fitting, in each pixel of Fe K-edge multiple energy μ-XRF maps of Fe^{II}-S, Fe^{II}CO$_3$, and Fe^{III}-(hydroxy)oxide microsites in the Fe^{III}-smectite sand synthetic core; (ii) The correlation curve(s) between both components being below the correlation curve(s) showing an ideal spatial distribution y=x (i.e. slope of 1, the dashed purple line), the cloud of points (i.e., pixels) that is near the correlation curve(s), including point below the curve(s), are selected to re-map component plotted in x-axis (i.e., the mask 5, 7, 9, and 11); (iii) The rest of the point are selected to re-map component plotted in y-axis (i.e., the mask 6, 8, 10, and 12). Comparison of the contribution spatial distribution map of the Fe components plotted in x-axis (iv) before and (v) after re-mapping using exclusively the points composing the mask in (ii). Comparison of the contribution spatial distribution map of the Fe components plotted in y-axis (vi) before and (vii) after re-mapping, using exclusively the points composing the mask in (iii).*

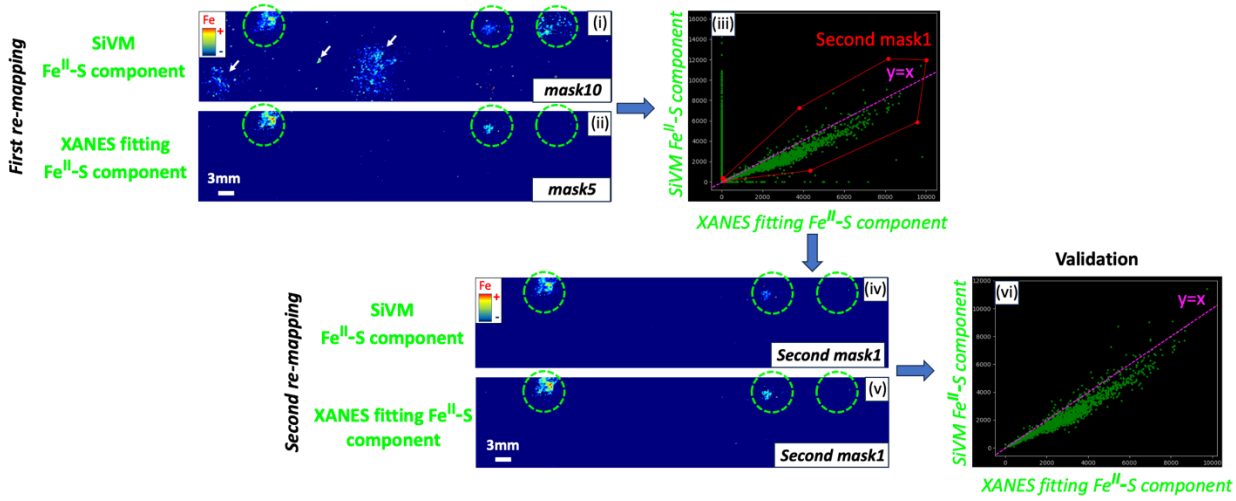

Figure SM-14. Second re-mapping of the spatial distribution of the Fe^{II}-S component contribution based on comparison of same re-mapped Fe component.

Top: *(i) and (ii): Comparison of the contribution spatial distribution map of the Fe^{II}-S component after a first re-mapping based on comparing of distinct Fe components (extracted from* ***Figure***

***SM-13 C and A**); (iii) Correlation plot of the contribution spatial distribution of two Fe^{II}-S components obtained from the 2 different paths of re-mapping described in (i) and (ii). A mask (outlined in red) is defined to select points (i.e., pixels) from the correlation plot for a second re-mapping of the contribution spatial distribution of the Fe^{II}-S components. Points excluded in the masking process are not linearly and simultaneously present in the two Fe^{II}-S component maps; (iv) and (v) Comparison of the spatial distribution map of the Fe^{II}-S component contribution plotted after a second re-mapping using exclusively the points composing the second mask in (iii); (vi) The second re-mapping of the contribution spatial distribution of the two Fe^{II}-S components are compared using correlation plot to verify that all points are perfectly correlated.*

*The dashed purple line (iii and vi) indicates an ideal spatial distribution y=x, i.e. a slope of 1, between the two re-mapping methods. **Note:** The false positive Fe^{II}-S microsites indicated by white arrows in the first re-mapping based on comparing distinct Fe components (i) were successively removed after the second re-mapping of the Fe^{II}-S components using exclusively the correlated points between two Fe^{II}-S component maps previously re-mapped a first time using 2 different paths (i.e., the second mask 1). The real locations of the Fe^{II}-S microsites are marked with green dashed circles.*

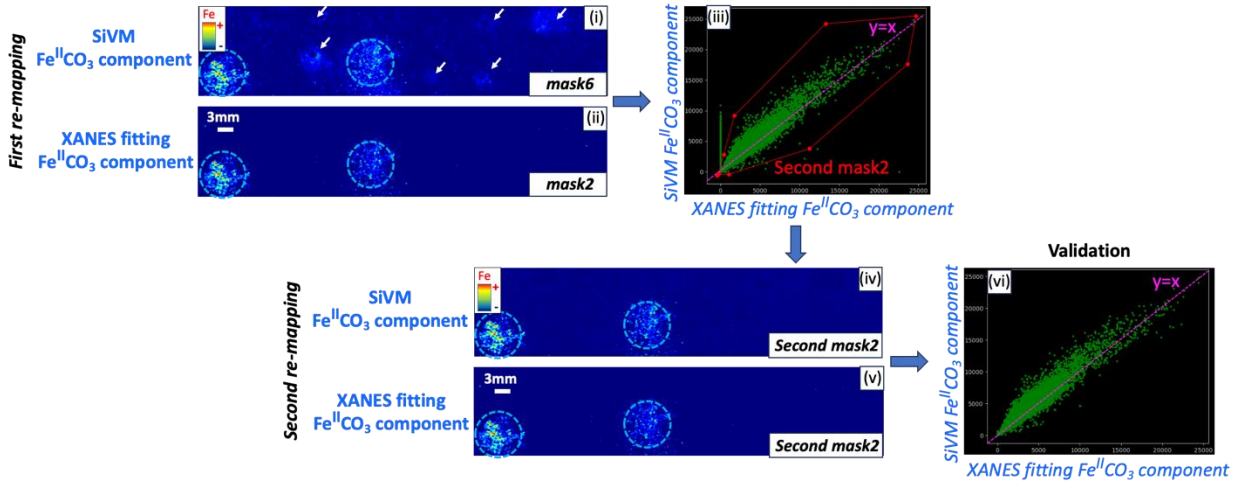

Figure SM-15. Second re-mapping of the spatial distribution of the $Fe^{II}CO_3$ component contribution based on comparison of same re-mapped Fe component..

***Top:** (i) and (ii): Comparison of the contribution spatial distribution map of the $Fe^{II}CO_3$component after a first re-mapping based on comparing distinct Fe components (extracted from **Figure SM-12 A and SM-13A**); (iii) Correlation plot of the contribution spatial distribution of two $Fe^{II}CO_3$ components obtained from the 2 different paths of re-mapping described in (i) and (ii). A mask (outlined in red) is defined to select points (i.e., pixels) from the correlation plot for a second re-mapping of the contribution spatial distribution of the $Fe^{II}CO_3$ components. Points excluded in the masking process are not linearly and simultaneously present in the two $Fe^{II}CO_3$ component maps; (iv) and (v) Comparison of the spatial distribution map of the $Fe^{II}CO_3$ component contribution plotted after a second re-mapping using exclusively the points composing the second mask in (iii); (vi) The second re-mapping of the contribution spatial distribution of the two $Fe^{II}CO_3$ components are compared using correlation plot to verify that all points are perfectly correlated.*

*The dashed purple line (iii and vi) indicates an ideal spatial distribution y=x, i.e. a slope of 1, between the two re-mapping methods. **Note:** The false positive Fe^{II}-S microsites indicated by white arrows in the first re-mapping based on comparing distinct Fe components (i) were successively*

removed after the second re-mapping of the $Fe^{II}CO_3$ components using exclusively the correlated points between two $Fe^{II}CO_3$ component maps previously re-mapped a first time using 2 different paths (i.e., the second mask 1). The real locations of the $Fe^{II}CO_3$ microsites are marked with green dashed circles.

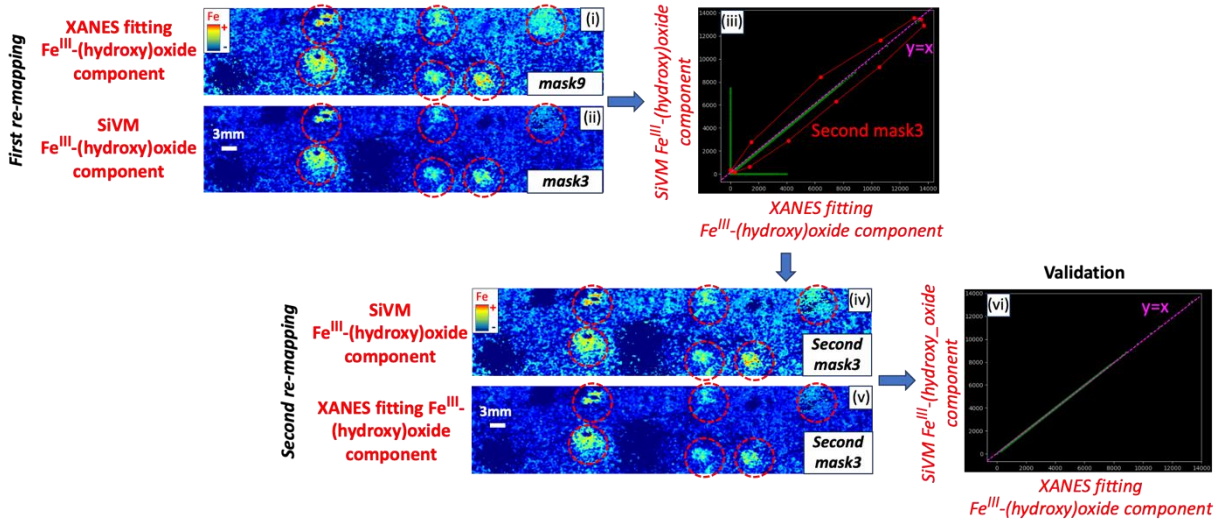

Figure SM-16. Second re-mapping of the spatial distribution of the Fe^{III}-(hydroxy)oxide component contribution based on comparison of same re-mapped Fe component.

Top: *(i) and (ii): Comparison of the contribution spatial distribution map of the Fe^{III}-(hydroxy)oxide component after a first re-mapping based on comparing distinct Fe components (extracted from **Figure SM-12A and SM-13A**); (iii) Correlation plot of the contribution spatial distribution of two Fe^{III}-(hydroxy)oxide components obtained from the 2 different paths of re-mapping described in (i) and (ii). A mask (outlined in red) is defined to select points (i.e., pixels) from the correlation plot for a second re-mapping of the contribution spatial distribution of the Fe^{III}-(hydroxy)oxide components. Points excluded in the masking process are not linearly and simultaneously present in the two Fe^{III}-(hydroxy)oxide component maps; (iv) and (v) Comparison of the spatial distribution map of the Fe^{III}-(hydroxy)oxide component contribution plotted after a second re-mapping using exclusively the points composing the second mask in (iii); (vi) The second re-mapping of the contribution spatial distribution of the two Fe^{III}-(hydroxy)oxide components are compared using correlation plot to verify that all points are perfectly correlated.*

The dashed purple line (iii and vi) indicates an ideal spatial distribution y=x, i.e. a slope of 1, between the two re-mapping methods. ***Note:*** *No false positive Fe^{III}-(hydroxy)oxide microsites indicated by white arrows in the top left panel(s) were detected, so, this step is technically not needed. However, when detecting redox microsites from natural samples, all steps have to be properly and systematically respected.* ***]***

References

Allard, T., Weber, T., Bellot, C., Damblans, C., Bardy, M., Bueno, G., Nascimento, N. R., Fritsch, E., and Benedetti, M. F. (2011). Tracing source and evolution of suspended particles in the Rio Negro Basin (Brazil) using chemical species of iron. *Chem. Geol.* 280, (1), 79-88.

Azoulay, I., Rémazeilles, C., and Refait, P., (2012). Determination of standard Gibbs free energy of formation of chukanovite and Pourbaix diagrams of iron in carbonated media. *Corros. Sci.* 58, 229-236.

Bone, S. E., Bargar, J. R., and Sposito, G., (2014). Mackinawite (FeS) Reduces Mercury(II) under Sulfidic Conditions. *Environ. Sci. Technol.* 48, (18), 10681-10689.

Cosmidis, J., Benzerara, K., Morin, G., Busigny, V., Lebeau, O., Jézéquel, D., Noël, V., Dublet, G., and Othmane, G. (2014). Biomineralization of iron-phosphates in the water column of Lake Pavin (Massif Central, France). *Geochim. Cosmochim. Acta* 126, 78-96.

Dublet, G., Juillot, F., Morin, G., Fritsch, E., Fandeur, D., Ona-Nguema, G., and Brown, G. E. (2012). Ni speciation in a New Caledonian lateritic regolith: A quantitative X-ray absorption spectroscopy investigation. *Geochim. Cosmochim. Acta* 95, 119-133.

Farges, F., Lefrere, Y., Rossano, S., Berthereau, A., Calas, G., and Brown, Jr., G. E. (2004). The effect of redox state on the local structural environment of iron in silicate glasses: a combined XAFS spectroscopy, molecular dynamics, and bond valence study. *J. Non Crystal. Solids* 344, 176-188.

Galoisy, L., Calas, G., and Arrio, M. (2001). High-resolution XANES spectra of iron in minerals and glasses: structural information from the pre-edge region. *Chem. Geol.* 174, 307-319.

Hohmann, C., Morin, G., Ona-Nguema, G., Guigner, J.-M. Brown, G. E., and Kappler, A. (2011). Molecular-level modes of As binding to Fe(III) (oxyhydr)oxides precipitated by the anaerobic nitrate-reducing Fe(II)- oxidizing Acidovorax sp. strain BoFeN1. *Geochim. Cosmochim. Acta* 75, (17), 4699-4712.

Kumar, N., Lezama Pacheco, J., Noel, V., Dublet, G., and Brown, G. E. (2018). Sulfidation mechanisms of Fe(iii)- (oxyhydr)oxide nanoparticles: a spectroscopic study. *Environ. Sci.: Nano* 5, (4), 1012-1026.

Maillot, F., Morin, G., Wang, Y., Bonnin, D., Ildefonse, P., Chaneac, C., and Calas, G. (2011). New insight into the structure of nanocrystalline ferrihydrite: EXAFS evidence for tetrahedrally coordinated iron(III). *Geochim. Cosmochim. Acta* 75, (10), 2708-2720.

Maillot, F., Morin, G., Juillot, F., Bruneel, O., Casiot, C., Ona-Nguema, G., Wang, Y., Lebrun, S., Aubry, E., Vlaic, G., and Brown, G. E. (2013). Structure and reactivity of As(III)- and As(V)-rich schwertmannites and amorphous ferric arsenate sulfate from the Carnoulès acid mine drainage, France: Comparison with biotic and abiotic model compounds and implications for As remediation. *Geochim. Cosmochim. Acta* 104, 310-329.

Morin, G., Noël, V., Menguy, N., Brest, J., Baptiste, B., Tharaud, M., Ona-Nguema, G., Ikogou, M., Viollier, E., and Juillot, F. (2017). Nickel accelerates pyrite nucleation at ambient temperature. *Geochem. Perspect. Lett.* 5, 6-11.

Noël, V., Marchand, C., Juillot, F., Ona-Nguema, G., Viollier, E., Marakovic, G., Olivi, L., Delbes, L., Gelebart, F., and Morin, G. (2014). EXAFS analysis of iron cycling in mangrove sediments downstream a lateritized ultramafic watershed (Vavouto Bay, New Caledonia). *Geochim. Cosmochim. Acta* 136, 211-228.

Ona-Nguema, G., Morin, G., Juillot, F., Calas, G., and Brown, G. E. (2005). EXAFS Analysis of Arsenite Adsorption onto Two-Line Ferrihydrite, Hematite, Goethite, and Lepidocrocite. *Environ. Sci. Technol.* 39, (23), 9147-9155.

Ona-Nguema, G., Morin, G., Wang, Y., Menguy, N., Juillot, F., Olivi, L., Aquilanti, G., Abdelmoula, M., Ruby, C., Bargar, J. R., Guyot, F., Calas, G., and Brown, G. E. (2009). Arsenite sequestration at the surface of nano-$Fe(OH)_2$, ferrous-carbonate hydroxide, and green-rust after bioreduction of arsenic-sorbed lepidocrocite by Shewanella putrefaciens. *Geochim. Cosmochim. Acta* 73, (5), 1359-1381.

Othmane, G., Allard, T., Morin, G., Sélo, M., Brest, J., Llorens, I., Chen, N., Bargar, J. R., Fayek, M., and Calas, G. (2013). Uranium Association with Iron-Bearing Phases in Mill Tailings from Gunnar, Canada. *Environ. Sci. Technol.*, 47, (22), 12695-12702

Pantke, C., Obst, M., Benzerara, K., Morin, G., Ona-Nguema, G., Dippon, U., and Kappler, A. (2012). Green Rust Formation during Fe(II) Oxidation by the Nitrate-Reducing Acidovorax sp. Strain BoFeN1. Environ. Sci. Technol., 46, (3), 1439-1446.

Trusiak, A., Treibergs, L. A., Kling, G. W., and Cory, R. M. (2018). The role of iron and reactive oxygen species in the production of CO2 in arctic soil waters. Geochim. Cosmochim. Acta, 224, 80-95.

Wang, S., and Mulligan, C. N. (2008). Speciation and surface structure of inorganic arsenic in solid phases: A review. Environ. Int., 34, (6), 867-879.

Westre, T. E., Kennepohl, P., DeWitt, J. G., Hedman, B., Hodgson, K. O., and Solomon, E. I. (1997). A Multiplet Analysis of Fe K-Edge 1s → 3d Pre-Edge Features of Iron Complexes. J. Am. Chem. Soc. 119(27), 6297–6314.

Wilke, M., Farges, F., Petit, P. E., Brown, Jr., G. E., and Martin F. (2001). Oxidation state and coordination of Fe in minerals: an Fe K- XANES spectroscopic study. *Am. Mineral.* 86(1998), 714-730.

EXAFS material (2023). https://static1.squarespace.com/static/655e3b72ac3ff440a8392450/t/6583a4c9e581504d041948ab/1703126218311/ReferenceSpectra_2023.pdf.